Physiologically engineered porous titanium/brushite scaffolds for critical-size bone defects: A design and manufacturing study

Dina Abdulaziz [a,*], Antonios D. Anastasiou [b], Vasiliki Panagiotopoulou [c], El Mostafa Raif [d], Peter V. Giannoudis [e], Animesh Jha [a]

[a] School of Chemical and Process Engineering, University of Leeds, Leeds, LS2 9JT, UK
[b] Department of Chemical Engineering, University of Manchester, Manchester, M1 3AL, UK
[c] Laboratory for Manufacturing Systems and Automation, University of Patras, 26504, Greece
[d] Faculty of Medicine and Health, School of Dentistry, University of Leeds, Leeds, LS2 9JT, UK
[e] Academic Department of Trauma and Orthopaedic Surgery, School of Medicine, University of Leeds, Leeds, LS2 9JT, UK

ARTICLE INFO

ABSTRACT

Repairing critical-size bone defects still represents a critical clinical challenge in the field of trauma surgery. This study focuses on a physiological design and manufacturing of porous composite scaffold (titanium Ti with 10 % mole iron doped brushite DCPD-Fe^{3+}) which can mimic the biomechanical properties of natural cortical bone, specifically for the purpose of repairing critical-size defects. To achieve this, the principle of design of experiments (DOE) was applied for investigating the impact of sintering temperature, mineral ratio, and volume fraction of porosity on the mechanical properties of the fabricated scaffolds. The fabricated scaffolds had open porosity up to 60 %, with pore size approximately between 100 μm and 850 μm. The stiffness of the porous composite scaffolds varied between 3.30 GPa and 20.50 GPa, while the compressive strength ranged from approximately 130 MPa–165 MPa at sintering temperatures equal to or exceeding 1000 °C. Scaffolds with higher porosity and mineral content demonstrated lower stiffness values, resembling natural bone. Numerical simulation was employed by Ansys Workbench to investigate the stress and strain distribution of a critical size defect in mid-shaft femur which was designed to be replaced with the fabricated scaffold. The fabricated scaffolds showed flexible biomechanical behaviour at the bone/scaffold interface, generating lower stress levels and indicating a better match with the femoral shaft stiffness. The experimental and numerical findings demonstrated promising applications for manufacturing a patient-specific bone scaffold for critical and potentially large defects for reducing stress shielding and minimizing non-union risk.

1. Introduction

Bone trauma cases have experienced a significant increase over the past few decades, and this can be attributed to several factors. These factors include the ageing population, lifestyle changes such as decreased physical activity, and the prevalence of osteoporosis (Tang et al., 2016; Amini et al., 2012). According to the UK National Hip Fracture Database, the cost of treating hip fractures alone is approximately £1 billion annually for the UK government and social care (National Hip Fracture Database, 2017, 2018, 2019; Johansen et al., 2014; Tyas et al., 2021). Fragility fractures resulting from osteoporosis affect over 300,000 patients in the UK each year and are estimated to cost around £4.4 billion (National Hip Fracture Database, 2019). Moreover,

statistical analysis suggests that the incidence of osteoporosis in Europe's ageing population will increase to 33.9 million in 2025 compared to 27.5 million in 2010, representing a 23% rise (Amini et al., 2012; Svedbom et al., 2013; Mozafari et al., 2019). This exponential increase in bone defects caused by trauma, disease, or injury has resulted in high demand for more advanced treatments to promote bone healing and reduce the associated health and economic burdens.

Bone tissue possesses remarkable regenerative capability, but the healing process can be negatively impacted by patients' underlying health and post-surgical complications (Giannoudis et al., 2007, 2008; Calori et al., 2011). These complications can manifest as delayed healing (delayed union), compromised union (malunion) or non-union. Treating these issues may necessitate multiple surgical interventions, resulting in

---

increased overall costs and discomfort for the patient (Kanis et al., 2000). Notably, critical-size defects pose a particular challenge, as they exceed the body's natural ability to heal spontaneously and require further surgical intervention (Walsh et al., 2017; Fallah et al., 2022; Voss et al., 2022; Nauth et al., 2018). These bone defects are typically defined as exceeding 2–2.5 times the diameter of the affected bone, with their incidence ranging from 0.4% to 11.4% (Giannoudis et al., 2016; Zhao et al., 2023). Despite advancements in surgical techniques and tissue regeneration procedures, treating critical-size bone defects remains a formidable task (Giannoudis et al., 2016; Woloszyk et al., 2023; Liu et al., 2022; Zhang et al., 2022). When a bone defect exceeds the critical size threshold, more complex surgical approaches and additional support are required, such as adding autologous bone fillers to enhance the chances of successful recovery (Schemitsch, 2017; Miller et al., 2016). However, the success of this treatment approach may not always be guaranteed, particularly in cases involving osteoporotic patients whose bone quality and quantity are compromised (Fallah et al., 2022; Arrington et al., 1996; Elsalanty et al., 2009). An alternative to autologous grafts is to use allografts, which utilise cadaver bone from bone tissue banks, or xenografts which use animal bone (Moreno et al., 2016; Chiarello et al., 2013; Nazirkar et al., 2014). However, these procedures carry a higher risk of infection due to the foreign body immune response at the recipient's site (Moreno et al., 2016; Zimmermann et al., 2011). Consequently, there is an urgent demand for alternative synthetic substitutes which can promote bone healing without the associated risks.

The first realization of the need for synthetic bone substitutes emerged after World War II when stainless steel and cobalt-based alloys gained popularity and used to aid victims of bone injuries (Chen et al., 2015; Ibrahim et al., 2017). Over time, titanium and titanium alloys have replaced stainless steel and cobalt alloys in many applications (Davis, 2003a; Bansiddhi et al., 2008). However, despite the advantages of titanium scaffolds, they still have limitations when it comes to bone regeneration. The limited osseointegration is a notable restriction, as this is essential for ensuring the long-term success of the scaffold. Research remains active in addressing the lack of osseointegration in titanium alloy scaffolds. Various strategies are being explored, including modifying the surface of implants and applying coatings that promote better integration with the surrounding bone tissue. For instance, bioactive coatings can be utilized to stimulate bone cell activity and encourage osseointegration (Clavell et al., 2016; Levine et al., 2010). These coatings often contain materials such as calcium phosphates (CaPs) and hydroxyapatite (HA), which mimic the composition of natural bone, or other substances that promote bone growth and attachment (Zhao et al., 2023; Clavell et al., 2016; Levine et al., 2010; Floroiana et al., 2007; Teimoori et al., 2023; Hubbe et al., 2022). Additionally, techniques like surface roughening or creating porous structures on the implant's surface can facilitate improved contact and interaction with the host bone (Levine et al., 2010; Schüpbach et al., 2005; Sidambe, 2014; Feller et al., 2014; Das et al., 2008). Despite the advancements in enhancing the osseointegration of titanium scaffolds, the significant challenge remains in minimizing the mismatch in mechanical properties between the scaffold and surrounding bone tissue. Titanium has a higher Young's modulus, indicating greater stiffness, compared to cortical bone (Moreno et al., 2016; Bansiddhi et al., 2014; Kramschuster et al., 2012; Dehghan-Manshadi et al., 2018; Chen et al., 2017a; Ghassemi et al., 2018; Yun et al., 2009). Depending on a patient's body mass index, the larger the magnitude of the mismatch stress, the greater the risk of stress shielding. In such a mechanical loading condition, the implant bears most of the mechanical load, leading to decreased stress on the surrounding bone, which results in incompatible physiological and anatomical conditions. Over time, this mechanical incompatibility can lead to bone loss via resorption (Moreno et al., 2016; Bansiddhi et al., 2014; Kramschuster et al., 2012; Dehghan-Manshadi et al., 2018; Chen et al., 2017a; Ghassemi et al., 2018; Yun et al., 2009).

Ceramic materials and bioglasses also find widespread use in the field of bone substitutes due to their known biocompatibility and corrosion resistance (Ibrahim et al., 2017; Hubbe et al., 2022; Bose et al., 2012; Piveteau et al., 1999; Kunisch et al., 2023). For instance, calcium phosphates (CaPs) are recognized for their superior osteoconductive properties, as their chemical characteristics closely resemble those of bone mineral. Furthermore, CaPs offer control over porosity which seem to be comparable with natural bone. Such morphological similarities between CaP and natural bone helps in bone remineralization and neo-osteogenesis by enhancing osteoblast activity when compared with the performance of standard hydroxyapatite (HAp) (Piveteau et al., 1999; Hench et al., 2015; Wang, 2004; Ma et al., 2016). However, the main limitation of CaPs is their low fracture toughness, which restricts their use in load-bearing applications. Their inherent brittleness and porosity can initiate crack propagation (Piveteau et al., 1999; Davis, 2003b; Zhou et al., 2011), making them better suited for filling bone defects or serving as a coating for metallic scaffolds (Piveteau et al., 1999; Hench et al., 2015; Wang, 2004; Ma et al., 2016; Eliaz et al., 2017). To address the mechanical limitations of ceramic materials and bioglasses, researchers have explored combinations with other materials. Several studies have also investigated ceramic materials and bioglasses as coatings on metal scaffolds. These trials have shown positive effects on bone healing, but the mechanical properties of the scaffolds still cannot fully mimic those of natural cortical bone to minimize stress shielding (Clavell et al., 2016; Levine et al., 2010; Hubbe et al., 2022).

In this work, the goal is to design and manufacture a physiologically biocompatible scaffold suitable for load-bearing applications, which supports bone healing specially in case of repairing critical-size defects. The scaffold design incorporates the principles of the "diamond concept", which serves as a conceptual framework for developing advanced treatments that enhance successful bone repair (Gorth et al., 2011). The diamond concept emphasises the significance of designing an optimal biomechanical environment in combination with osteo-inductive, conductive and angiogenesis. Only when these four anatomical and physiological functions prevail, bone will be able to heal at the fracture site (Amini et al., 2012; Kramschuster et al., 2012; Ghassemi et al., 2018; Bose et al., 2012; Ma et al., 2016; Liverani et al., 2017; Liu et al., 2014; O'brien, 2011; Andrzejowski et al., 2019). This study has focused for the first time on physiological design and fabrication of porous titanium/brushite scaffolds that can reduce stress shielding in critical size bone defects. The mechanical properties of the scaffold are influenced by various fabrication conditions, and therefore, this research has concentrated on the key synthesis variables: i) sintering temperature, ii) mineral ratio, and iii) porosity. A design of experiments approach was followed to systematically investigate and define the range and combination of values that would yield mechanical properties similar to those of a natural cortical bone. In addition to experimental investigations, the finite element analysis was employed to simulate the mechanical behaviour of critical size defect in mid shaft femur which was replaced with the fabricated scaffolds. The analysis's objective is to understand the interactions between the fabricated scaffolds and the surrounding bone, with a focus on gaining insights into stress mismatch and stress shielding.

2. Materials and methods

2.1. Mineral synthesis

A 10% mole Fe^{3+} doped brushite (DCPD-Fe) with a Ca:P ratio of 1:1 was synthesised using precipitation method previously described in literature (Anastasiou et al., 2016, 2017; Elmadani et al., 2012; Toshima et al., 2014; Alsubhe et al., 2020). A 10% mole of $Fe(NO_3)_3 \cdot 9H_2O$ powder (VWR Chemicals, CAS: 7782-61-8) was added to a 200 mL, 0.1 M $Ca(NO_3)_2 \cdot 4H_2O$ solution (Fisher Chemicals, CAS:13477-34-4), and the resulting mixture was heated to 37 °C. Subsequently, 200 mL of a 0.1 M $HPO_4(NH_4)_2$ solution (Acros Organics, CAS:7783-28-0) was added dropwise, while continuously stirring the mixture at 37 °C for 2 h. The final mixture was then allowed to stand for an additional hour without

heating to allow for precipitation. The brushite crystals that formed were collected on a filter paper with 3 μm pores (Whatman grade 44), washed with distilled water several times, and dried in an air furnace at 80 °C for 24 h.

2.2. Scaffolds design and manufacturing

The study employed Design of Experiments (DOE) principles to investigate the impact of mineral content, porosity level, and sintering temperature on the mechanical properties of the fabricated scaffolds. The design involved three variables (sintering temperature, porosity, and mineral ratio), each with three levels as outlined in Table 1, which resulted in 13 different samples. The scaffolds were fabricated using the powder metallurgy with space holder process. Varying ratios (0, 5, 10 vol%) of the synthesised mineral (DCPD-Fe) were mixed with titanium powder (Ti, 99.7% purity, Sigma Aldrich ® 268496), and the porosity was controlled by adjusting the volume ratio of potassium chloride (KCl, 99.1% purity, Fisher Chemical) (0, 20, 40 vol%) to the titanium and brushite mixtures (Table 2). Scanning Electron Microscope (SEM) images were taken to show the particles' morphology of the different powders used in the study (Fig. 1). In Fig. 1a and b, the microscopic evidence of the particle size ranges for Ti powder (45–180 μm) and KCl powder (100–400 μm), respectively are shown. The different powder combinations were uniaxially pressed at 250 MPa at room temperature using a manual hydraulic press with a closed stainless-steel die to produce cylindrical samples measuring 10 mm in diameter and 10 mm in height. The samples were then immersed in heated water at 80 °C for 3 h to dissolve and remove the KCl space holder. Afterwards, each sample was washed and cleaned with isopropanol in an ultrasonic bath for 1 h and then dried in an air furnace at 90 °C for 3 h before undergoing thermal sintering in an argon atmosphere. Three different sintering temperatures (850°, 1000°, 1150 °C) were used, with a constant time of 2 h and a heating/cooling rate of 15 °C/min.

2.3. Characterization techniques

2.3.1. Simultaneous thermal analysis (STA)

The phase transformation of the Fe^{3+} doped brushite powder was investigated using the STA technique (PerkinElmer®, STA 8000). All thermal experiments were conducted in a nitrogen atmosphere, and alumina powder (Al_2O_3) was utilized as a reference. Approximately 10 mg of the tested powder was used for each experiment. The temperature range of the instrument spanned from ambient to 1450 °C. Initially, the sample was held at 30 °C for 1 min, after which it was heated up to 1450 °C at a rate of 20 °C/min. The sample was then kept at 1450 °C for 1 min before being cooled down to 30 °C at a rate of 20 °C/min.

2.3.2. X-ray diffraction (XRD)

The phase composition of the synthesised composite material (titanium with 10% vol Fe^{3+} dopped brushite) was analysed using a Bruker D8 X-ray diffractometer, Billerica, MA, USA. The diffractometer was equipped with a monochromatic Cu K_{α} radiation source ($\lambda = 1.54$ Å) and operated at a voltage of 40 kV. The samples were analysed within a Bragg angle (2θ) scanning range of 5°–80°, with a scan speed of 1° s^{-1} and a step size of 0.065°. The resulting patterns were analysed using a High Score Plus software (PANalytical X'Pert HighScore Plus v3.0, Malvern, UK).

Table 1
The three levels of the variables used in the study.

Variable	Level		
	Low (−1)	Medium (0)	High (+1)
Sintering Temperature (°C)	850	1000	1150
Porosity (KCl vol%)	0	20	40
Mineral ratio (vol%)	0	5	10

Table 2
A list for the designed and manufactured scaffolds.

Designed Scaffolds		
Sample code[a]	KCl (vol%)	DCPD-Fe (vol%)
(0,0)	0	0
(0,5)	0	5
(0,10)	0	10
(20,0)	20	0
(20,5)	20	5
(20,10)	20	10
(40,0)	40	0
(40,5)	40	5
(40,10)	40	10

[a] Samples named as following (KCl vol%, DCPD-Fe vol%), for example (20,5) means the sample containing 20 vol% of KCl and 5 vol% of DCPD-Fe.

2.3.3. Helium pycnometer

The helium pycnometer (Pycnomatic ATC, Thermofisher Scientific) was utilized to measure the density and open porosity of the synthesised scaffolds. This method was chosen due to the high diffusivity of helium, which allows it to penetrate even the smallest pores in the scaffold structure, resulting in highly accurate porosity estimations. Additionally, the technique offers excellent temperature control to prevent any volume changes during the measurement process (Yang et al., 2017; Webb, 2001). The procedure involved taking repeat measurements for each sample until three density values were obtained with a standard deviation of less than 0.5%. Triple samples for each composition were utilized, and the average of the values obtained was calculated.

2.3.4. Scanning Electron Microscope (SEM) and energy-dispersive X-ray spectroscopy (EDX)

The morphology of the materials and scaffolds, as well as the pore size and shape of the porous scaffolds, were examined using Scanning Electron Microscopy (Hitachi SU8230 1–30 kV cold field emission gun, Düsseldorf, Germany). An Oxford Instruments 80 mm^2 SD detector was equipped on the microscope for Energy Dispersive X-ray Spectroscopy, and Aztec processing software was utilized to identify the elemental composition of the synthesised composite material.

2.3.5. Micro computed tomography (μCT)

Micro computed tomography (Skyscan 1172, Bruker, Belgium) (μCT) was employed to examine the porous scaffolds. However, this analysis can be challenging for metal samples due to the attenuating X-rays and may result in dark and bright grainy artefacts that obscure details in the scan images (Ho et al., 2006; Tuan et al., 2007). Moreover, the results are dependent on the applied algorithms and setups, which can lead to approximate results with minor errors. To mitigate these challenges, the samples were characterised in different planes, and hundreds of cross-sections were recorded in three directions. The X-ray source was controlled at a constant voltage of 100 kV and 100 μA current, and two filters of 0.5 mm aluminium were used. The scanning process involved a rotational step of 0.4° and a total scanning time of 80 min, which resulted in 1400 2D slices being recorded. The image resolution was 10 μm. The 3D scaffold structure was reconstructed from the 2D projection images using Nrecon, SkyScan software, and the analysis was performed using Dragon Fly software version 2020.2.0.941.

2.4. Mechanical testing

The study was conducted to investigate the influence of each synthesis parameter and their interactions on the mechanical properties of the scaffolds. The mechanical properties of the 13 synthesised scaffolds were initially calculated from stress-strain curves obtained through compression testing using an INSTRON 5569 test machine. The testing was conducted according to ASTM E9-89a at a crosshead speed of 0.001 mm/s in the longitudinal direction at room temperature. The testing was
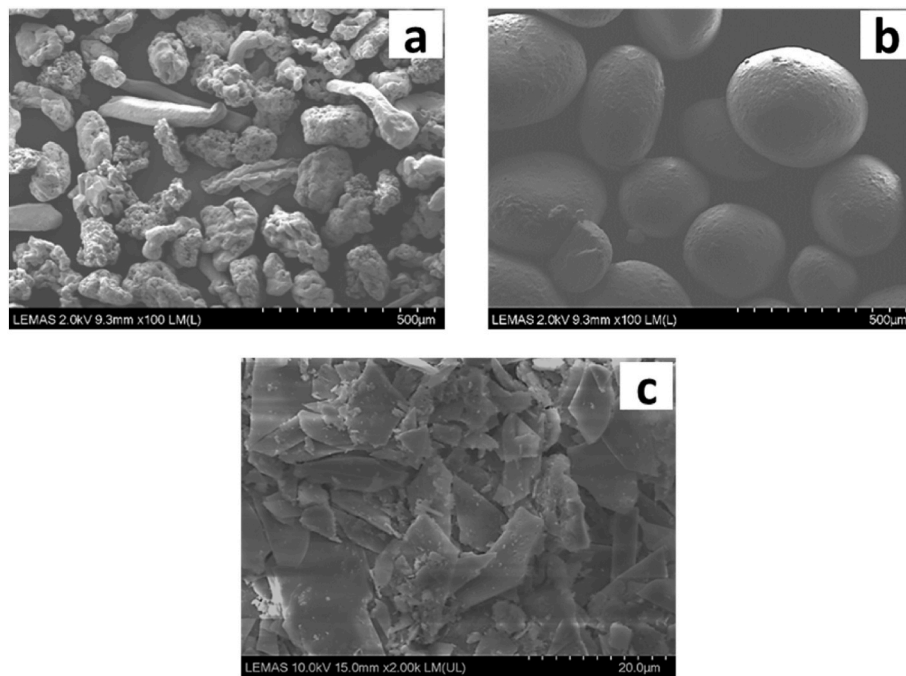
Fig. 1. SEM images for titanium powder (Ti) (a), potassium chloride powder (KCl) (b) and the synthesised 10% mole Fe^{3+} doped brushite powder (DCPD-Fe) (c).

performed three times (n = 3) to ensure the statistical variance and error distribution. Then the optimisation study was performed using Minitab 21.2 software, creating a three-factor Box-Behnken Design (BBD). The experimental data were fitted using a second-order polynomial regression model represented by Eq (1), considering the number of variables and levels:

$$Y = a_0 + \sum_{i=1}^{3} a_i X_i + \sum_{i=1}^{3} a_{ii} X_i^2 + \sum_{i=1}^{2} \sum_{j>1}^{3} a_{ij} X_i X_j \tag{1}$$

where, Y represents the response (Young's modulus, compressive strength or yield stress). a_0, a_i, a_{ii}, and a_{ij} are the regression coefficients for intercept, linear, quadratic and interaction terms, respectively. X_i and X_j are the independent variables (factors).

2.5. Numerical study

The finite element analysis using ANSYS WORKBENCH 2020 R1 was carried out to investigate the mechanical behaviour of a critical size defect in mid-shaft femur which was designed to be replaced with the fabricated scaffold. The femur bone carries a significant portion of the body weight during daily activities, providing crucial support to the human body (Sheikh et al., 2016; Kumar et al., 2015; Bhosale et al., 2013). Fractures in the femur can occur in various regions but this analysis considered femoral shaft fractures, as they are among the most common femoral injuries that require careful attention due to the load-bearing nature of the site (Sheikh et al., 2016; Lowe et al., 2018; Bergh et al., 2020). An already established and validated model of human femur bone was used for the computational study (Mahmoudi, 2017). Then a critical size defect of 5 cm was modelled and filled with a cylindrical scaffold (Fig. 2). The study assumed that bone is a homogeneous, isotropic, and linearly elastic material with a density of 2000 kg/m^3, Young's Modulus of 12 Gpa, and Poisson's ratio of 0.33 (Sheikh et al., 2016). In contrast, the experimental density and mechanical properties were used for the synthesised scaffolds in the numerical analysis. The simulation considered a healthy male with an average body weight of 85 kg, and the boundary conditions consisted of applying a compressive load equivalent to the weight of the body on the femoral head and fixing the distal end of the femur, which represents the support provided by the knee joint (Qasim et al., 2016; Yousif et al., 2012). The models were meshed using tetrahedral meshing (Sheikh et al., 2016), and the solution was done three times by increasing the number of elements to get better results. Proper settings and values were executed to use more minor elements on proximities and curvatures for the model (Yousif et al., 2012).

3. Results

3.1. Simultaneous thermal analysis

The phase transformation temperatures of Fe^{3+} doped brushite powder during heating were investigated using differential scanning calorimetry (DSC) and thermogravimetry analysis (TGA). The synthesised powder was heated at a constant rate of 20 °C/min within a temperature range of 30 °C–1450 °C (McIntosh et al., 1956). Weight and enthalpy changes were recorded during heating and five stages of decomposition were observed. The first transformation occurred at ~204 °C resulting in the loss of two water molecules and transformation into monetite (CaHPO$_4$) (Eq. (2)). Upon heating to ~470 °C, the second transformation occurred, leading to the formation of γ-pyrophosphate (γ-Ca$_2$P$_2$O$_7$) following the reaction in (Eq. (3)) with a reduction in weight due to the loss of ½ H$_2$O during the heating cycle. The exothermic peak at ~715 °C corresponds with the formation of β-pyrophosphate (β-Ca$_2$P$_2$O$_7$), which eventually changed at 1050 °C to α-pyrophosphate (α-Ca$_2$P$_2$O$_7$). The onset of the melting of α-Ca$_2$P$_2$O$_7$ begins at ~1294 °C. The overall weight loss in the mineral weight was found to be of the order of ~27%. It is evident that ~21% of the weight drop was due to water loss during the transformation of brushite to monetite, and another ~6% reduction took place during the formation of γ-pyrophosphate (γ-Ca$_2$P$_2$O$_7$). Fig. 3 depicts the recorded weight and enthalpy changes during the heating process.

$$2CaHPO_4 \bullet 2H_2O \xrightarrow{204°C} 2CaHPO_4 + 4H_2O \tag{2}$$

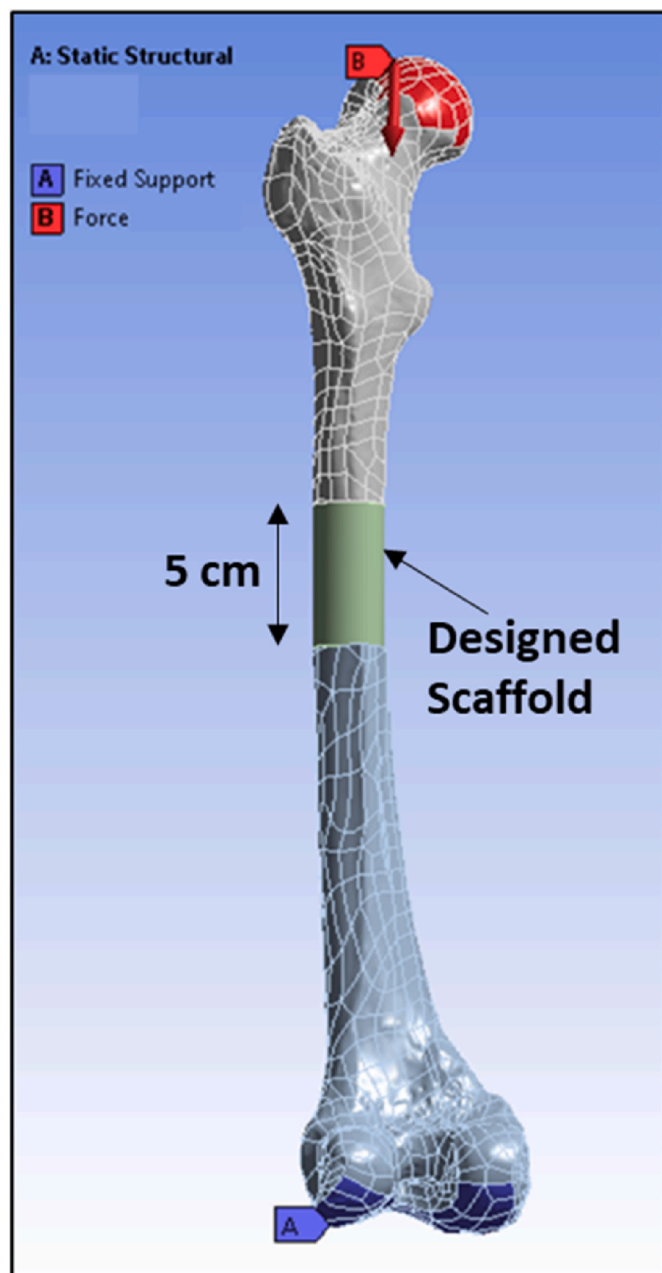$$2CaHPO_4 \xrightarrow{470°C} Ca_2P_2O_7 + H_2O \tag{3}$$
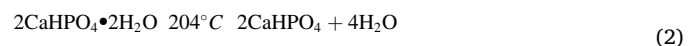
Fig. 2. The CAD model of a femur bone with 5 cm defect in the mid shaft. The defect was filled with a designed scaffold. The boundary conditions included applying a compressive force on the femoral head (in red) and fixed support at the distal part (in purple).

3.2. X-ray diffraction

Fig. 4 shows the XRD diffraction pattern of the composite material (titanium with 10% vol Fe^{3+} dopped brushite), sintered in argon at 1000 °C for 2 h. Based on the X-ray diffraction pattern of the composite material, it is evident that the material is composed of two phases: hexagonal α-titanium and β-pyrophosphate (β - $Ca_2P_2O_7$). The dominant phase identified in the pattern is hexagonal α-titanium, which is represented by the JCPDS 04-006-2824 card. The peaks observed at $2\theta°$ ~37.09°, 41.36°, 44.55°, and 46.30° correspond to β-pyrophosphate (β - $Ca_2P_2O_7$), which is represented by the JCPDS-00-017-0499 card. This finding is consistent with the phase transformation curve in Fig. 3, which suggests that γ to β transformation of DCPD-Fe powder occurred at 715 °C.
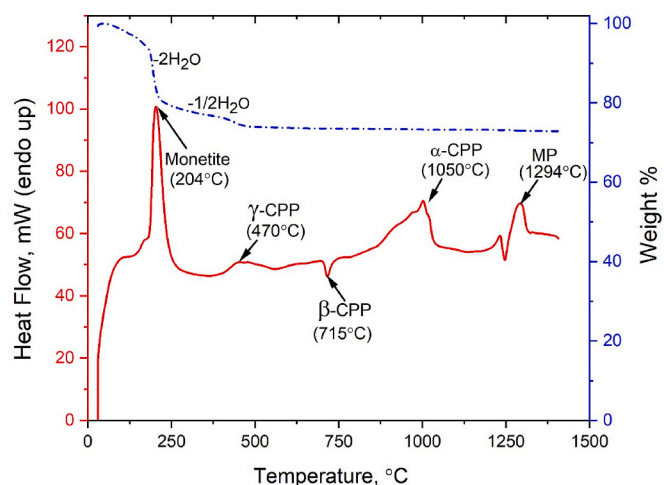

Fig. 3. Thermal analysis of the Fe^{3+} doped brushite (DCPD-Fe) powder, identifying the phase transformation during heating up to 1450 °C with a constant rate of 20 °C/m. The DSC curve is shown in red (values reported on the LH y-axis), and the TGA curve is shown in dash blue (values reported on the RH y-axis).

3.3. Helium pycnometer

Table 3 presents the apparent density, skeletal density, and open porosity of the synthesised scaffolds with different DCPD-Fe and KCl ratios. The apparent density was determined by measuring the mass and apparent volume of each sample. Skeletal density and open porosity were calculated using the helium pycnometer technique, with the values obtained using the following equations (4) and (5) (Dabrowski et al., 2010; Semel et al., 2006; Cheppudira Thimmaiah et al., 2018). The skeletal density (ρ) of scaffolds was calculated as the ratio of mass (M) to the measured skeletal volume ($V_{pycnometric}$), which refers to the volume of solid material containing closed pores. The helium pycnometer technique can only quantify the open porosity accessible to the helium. The open porosity (P_{open}) was defined as the ratio of the volume of open pores (V_{pore}) to the total volume (V_{total}).

$$\rho = \frac{M}{V_{\text{pycnometric}}} \tag{4}$$

$$P_{\text{open}} \ (\%) = \frac{V_{\text{pore}}}{V_{\text{total}}} = \frac{V_{\text{total}} - V_{\text{pycnometric}}}{V_{\text{total}}} \tag{5}$$

Samples of pure titanium, denoted as (0,0), were utilized as a benchmark to compare with composite and porous samples. The density of the pure titanium sample was 4.39 g/cm^3, and its open porosity was approximately 26%. When the volume fraction of the space holder (KCl) was increased, the porosity of scaffolds increased, and the apparent density decreased. The open porosity of samples (20,0) and (40,0) increased from 37.89% to 55.40%, respectively, indicating the successful removal of the space holder particles after immersion in heated water at 80 °C. By increasing the ratio of DCPD-Fe mineral from 5 vol% to 10 vol%, the open porosity of solid composite samples (0,5) and (0,10) increased from approximately 27.97%–29.41%, respectively. A similar trend was observed in samples (20,0), (20,5), and (20,10), with open porosity increasing from 37.89% to 38.65%. However, this influence was more pronounced in higher porous samples (40,0), (40,5), and (40,10), where the open porosity increased from 55.40% to 60.00% by increasing the mineral ratio from 0 to 10 vol%.

3.4. Scanning Electron Microscope and energy-dispersive X-ray spectroscopy

Fig. 5 illustrates the morphology and phase distribution in the
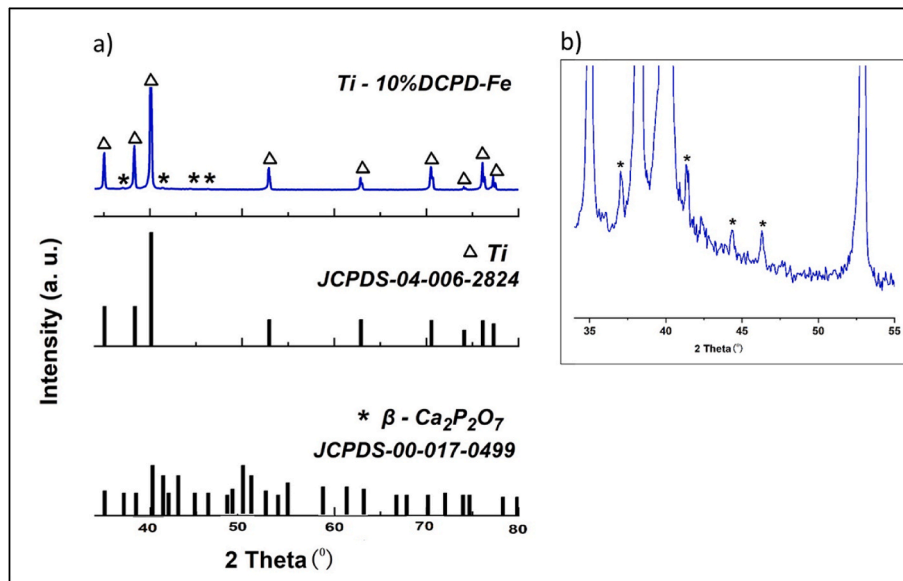
Fig. 4. X-ray diffraction pattern of the composite material (Ti with 10% vol DCPD-Fe) after sintering in argon at 1000 °C for 2 h, with indexing to the JCPDS reference files of titanium Ti (Δ) and β-pyrophosphate β - $Ca_2P_2O_7$ (*) (a). A magnified X-ray pattern highlighting the peaks associated with β-pyrophosphate phase (b).

Table 3
The mean values of density and open porosity of the synthesised scaffolds sintered in argon at 1000 °C for 2 h (n = 3).

Sample	Apparent density (g/cm^3)	Skeletal density (g/cm^3)	Open porosity (%)
(0,0)	3.25	4.39	25.96
(0,5)	3.09	4.29	27.97
(0,10)	3.00	4.25	29.41
(20,0)	2.72	4.38	37.89
(20,5)	2.60	4.20	38.09
(20,10)	2.54	4.14	38.65
(40,0)	1.94	4.35	55.40
(40,5)	1.88	4.30	56.28
(40,10)	1.68	4.20	60.00

composite material (titanium with 10 vol% Fe^{3+} dopped brushite) after sintering in an inert atmosphere at 1000 °C for 2 h. The microstructure had clear grain boundaries and was dominated by titanium, with the DCPD-Fe mineral distributed between the Ti-alloy grains. Fig. 5c displays the presence of tiny pores between Ti grains and DCPD-Fe particles. This finding confirms the helium pycnometer results indicating that open porosity increases with the presence of DCPD-Fe mineral. The SEM images in Fig. 6 depict porous composite scaffold (Ti with 10 vol% DCPD-Fe) that was fabricated using 40 vol% KCl as a space holder. Fig. 7 presents the elemental mapping of the composite scaffold (Ti with 10 vol % DCPD-Fe), which confirmed the distribution of DCPD-Fe mineral between titanium grains. The EDX analysis of composite scaffolds was carried out at various locations, and the overall EDX mapping demonstrated the presence of Titanium (Ti), Oxygen (O), Calcium (Ca), Phosphorus (P), and a minor amount of Iron (Fe). The EDX analysis confirmed the XRD data, indicating that there was no significant oxidation of titanium in the scaffold. Additionally, the EDX images revealed the uniform distribution of Fe over the structure. In the interface area, titanium and phosphorus (P) were detected, as shown in Fig. 7b, indicating that phosphorus diffusion into titanium particles occurred during the sintering process, which is consistent with the findings of the Balbinotti study (Balbinotti et al., 2011).

3.5. Micro computed tomography

Fig. 8 displays 2D μ-CT images of the porous titanium scaffolds (Ti with 10 vol% DCPD-Fe) fabricated using different ratios of KCl as space holder. Fig. 8a and b correspond to the composite scaffold (40,10) fabricated with 40 vol% KCl, while Fig. 8c and d belong to the composite scaffold (20,10) fabricated with 20 vol% KCl. Fig. 8a and c shows the top view cross-section (x, y-direction) and Fig. 8b and d shows the side view cross-sections (x, z-direction). As depicted in the top views, the spherical shape of the single pores is related to the shape of the initial space holder particles (KCl particles). Since the KCl crystals were entirely removed during the dissolution process, providing well-defined open pores that are apparent from the surface through to the centre of the scaffold. The scaffolds had large macropores, with an average size of 100–450 μm, as well as smaller pores (<50 μm) formed between pressed and sintered particles, which allowed for interconnectivity throughout the structure. The pores in the scaffold with only 20 vol% KCl appeared to be more self-isolated and closed, while the scaffolds with 40%vol KCl exhibited a higher level of aggregation, resulting in larger and more irregularly shaped pores (600–850 μm). The software analysis showed that the total porosity was approximately 47% for the (20,10) scaffold and 65% for the (40,10) scaffold. The interconnectivity of the pores was significantly increased in the 40%vol KCl scaffolds due to the aggregation of pore clusters. The porous scaffold with higher porosity (40,10) showed that most of the pores (~95%) were interconnected and accessible, as indicated in green in Fig. 8a and b whilst very few pores were inaccessible, as shown in red. However, the (20,10) scaffold displayed lower porosity and interconnectivity, with approximately 20% of pores being inaccessible, as depicted in Fig. 8c and d. These findings were consistent with the results obtained from the helium pycnometer method.

3.6. Mechanical properties

The theoretical models for the responses of Young's modulus, compressive strength, and yield stress are shown in Eqs (6)–(8), respectively. These models considered the effect of the synthesis variables and their interaction terms on the responses. The statistical analysis was carried out by implementing response surface methodology (RSM) using a three-factor Box-Behnken design (BBD). The regression equations were generated to describe the changes in the values of
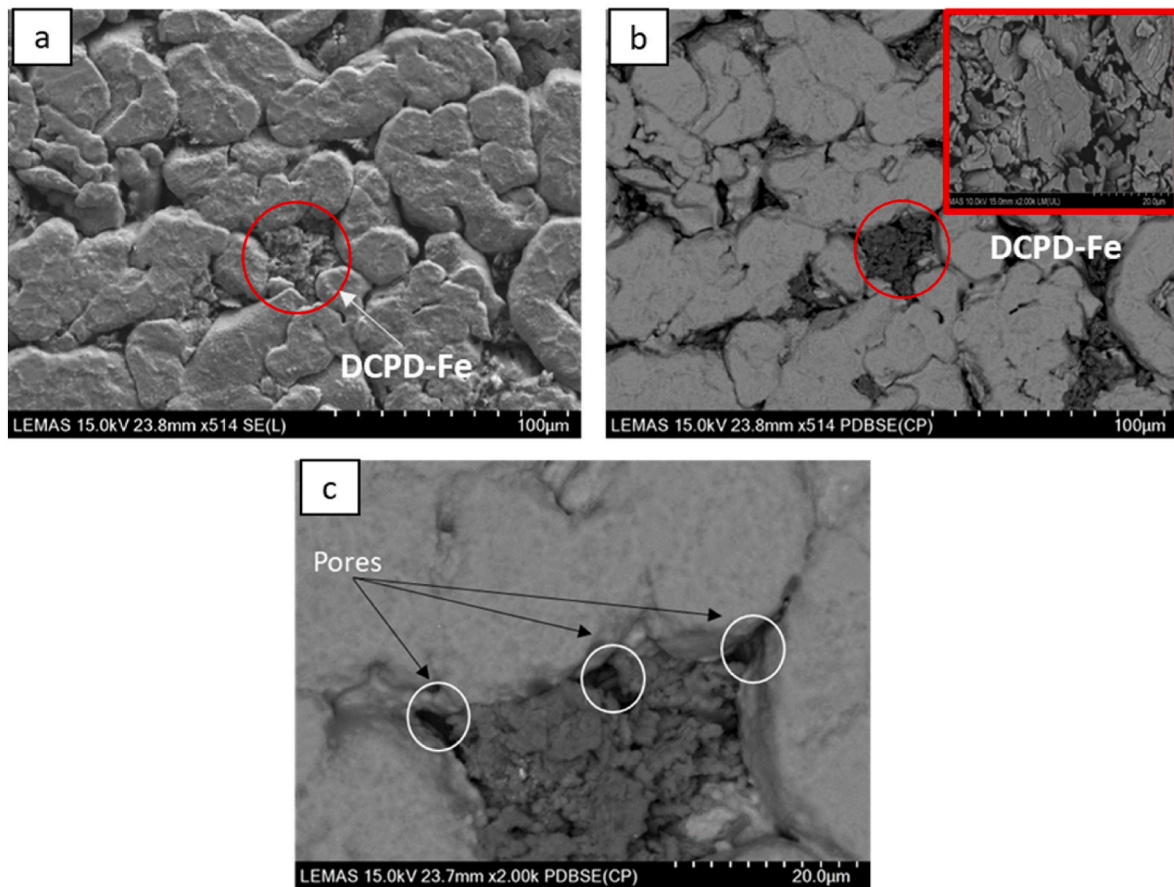
Fig. 5. SEM micrographs of the composite material (Ti with 10 vol% DCPD-Fe) (a & b). Magnified SEM image showing the pores between titanium grains and mineral particles (c).
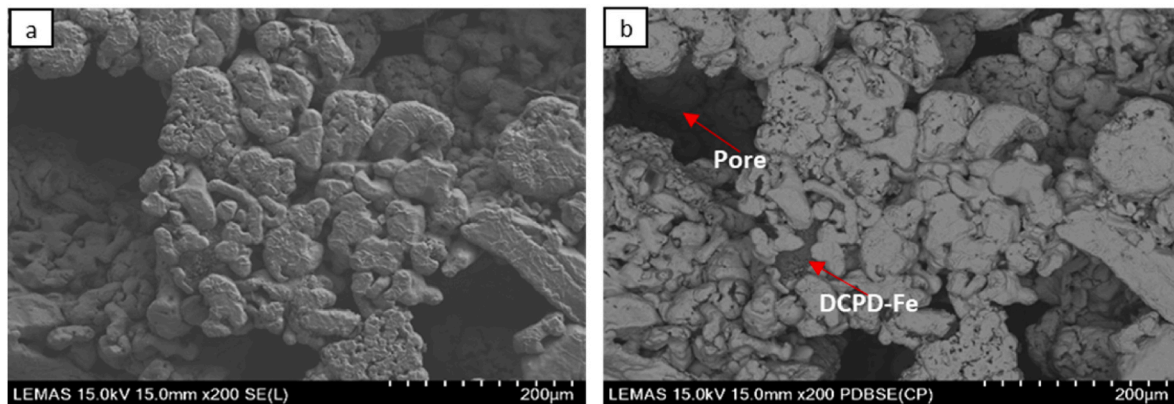

Fig. 6. SEM images of (40,10) scaffold; the porous composite scaffold (Ti with 10 vol% DCPD-Fe) fabricated using 40 vol% KCl.

Young's moduli, compressive strengths, and yield stresses in response to alterations in synthesis parameters, including sintering temperatures, porosity, and mineral ratio. The experimental values of the mechanical properties (responses) were entered corresponding to the input synthesis parameters (variables) in the created design matrix (He et al., 2012; Bhatt et al., 2015; Mandal et al., 2006). In the equations, A, B, and C represent the variables of sintering temperature, space holder, and mineral ratio, respectively. The R^2 values obtained were approximately 98%, indicating that the models could explain over 98% of the variations observed in the responses. Additionally, the adjusted determination coefficient (R^2 (adj) = 97.72%) confirmed the significance of the models.

$$\text{Young Modulus [GPa]} = -245.2 + 0.531A - 0.521B - 1.13C - 0.000248\,A{*}A + 0.00284\,B{*}B + 0.0196\,C{*}C - 0.000283\,A{*}B + 0.00007\,A{*}C + 0.0263\,B{*}C \tag{6}$$

$$\text{Compressive Strength [MPa]} = 321 + 0.49\,A - 37.00\,B - 11.6\,C - 0.000083\,A{*}A + 0.4909\,B{*}B + 1.245\,C{*}C + 0.00317\,A{*}B - 0.0157\,A{*}C + 0.225\,B{*}C \tag{7}$$

$$\text{Yield Stress [MPa]} = -955 + 2.248\,A - 7.73\,B + 7.7\,C - 0.000933\,A{*}A + 0.2319\,B{*}B - 0.410\,C{*}C - 0.00925\,A{*}B - 0.0003\,A{*}C - 0.1500\,B{*}C \tag{8}$$
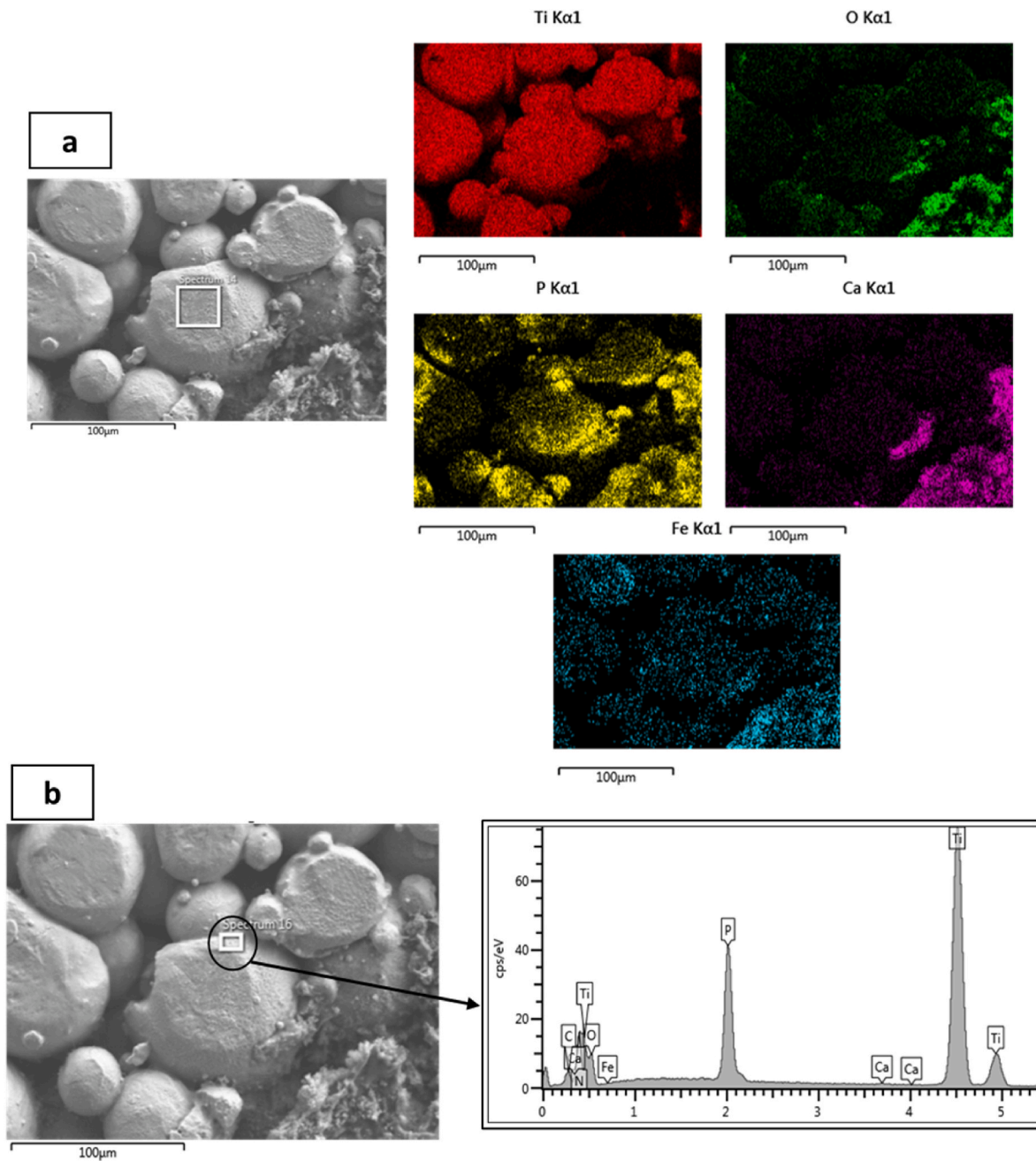
Fig. 7. EDX mapping of the composite scaffold (titanium with 10 vol% DCPD-Fe) illustrating the elemental composition (a). EDX analysis of the interface region showing the presence of titanium (Ti) and phosphorus (P) (b).

After obtaining the regression equations for the responses, a model reduction process was applied to eliminate the insignificant terms and simplify the models, thereby maximising the precision of predictions. The parameter $\alpha = 0.05$ was used as the threshold for statistical significance, and the p-value was used to check the relevance of each term. All the terms with p-value >0.05 were removed. The final reduced models of the mechanical properties are:

$$\text{Young Modulus [GPa]} = 0.3 + 0.0293 \, A - 0.5594 \, B \qquad (9)$$

$$\text{Compressive Strength [Mpa]} = 380.0 + 0.3092 \, A - 32.50 \, B - 10.32 \, C + 0.4857 \, B^2 \qquad (10)$$

$$\text{Yield Stress [Mpa]} = 176.3 + 0.1950 \, A - 17.95 \, B + 0.2375 \, B^2 \qquad (11)$$

The Pareto charts and normal plots were utilized to visualize the standardized effects of the synthesis parameters on the mechanical properties of the scaffolds. Fig. 9 shows the Pareto charts and normal plots for the compressive strength, Young modulus, and yield stress. The Pareto charts display the absolute values of the standardized effects in order of significance, with the dashed red line indicating the statistically significant effects at $\alpha = 0.05$ level. Longer bars indicate larger effects, while shorter bars indicate smaller effects. The normal plots assess the normality of the standardized effects, with the red squares representing significant influences on the response, and blue circles indicating nonsignificant impacts.

The 2D contour plots of the effect of the synthesis parameters on the mechanical properties are presented in Fig. 10, considering the variables with the most significant impact. Fig. 10a illustrates how the compressive strength was affected by the porosity and mineral ratio at a constant sintering temperature of 1150 °C. Fig. 10 b and c show the effect of
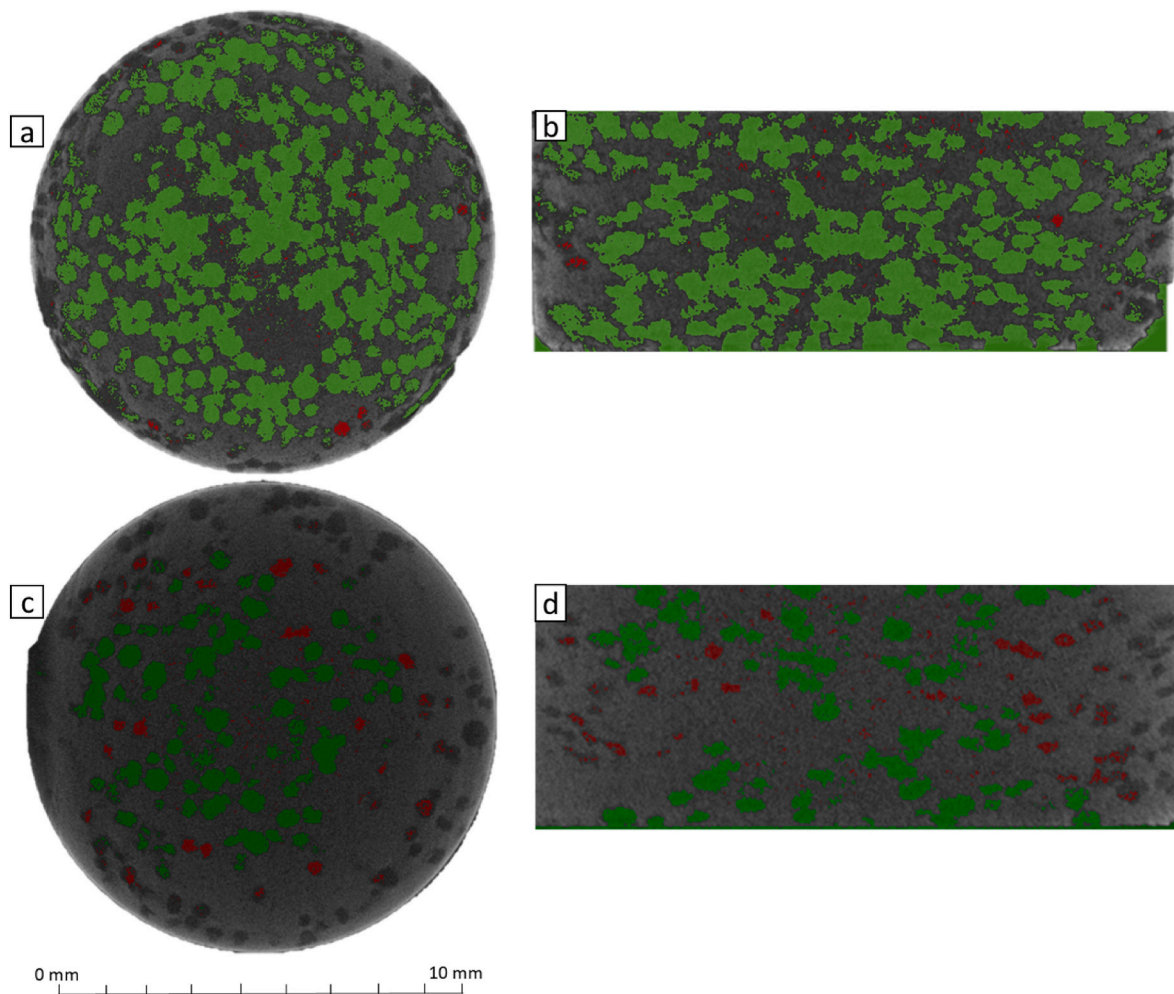
Fig. 8. μ-CT cross sections showing the accessible pores in green and inaccessible pores in red for the porous composite scaffolds (titanium with 10 vol% DCPD-Fe); (40,10) scaffold fabricated using 40 %vol KCl (a & b) and (20,10) scaffold fabricated using 20 %vol KCl (c & d).

porosity and sintering temperature on elastic modulus and yield stress at a constant mineral ratio of 10 vol%. The study found that increasing sintering temperature from 850° to 1150 °C resulted in an increase in elastic modulus, compressive strength, and yield stress. Fig. 10a showed that porosity had a negative contribution to compressive strength, especially when the KCl fraction was higher than 20%. Increasing the mineral ratio from 0 to 10 vol% for the scaffolds with the same designed porosity (20 vol% KCl) and sintered at the same temperature resulted in a significant reduction in the ultimate compressive strength. For instance, the compressive strength of the (20,0) and (20,10) scaffolds sintered at 1150 °C were 340 MPa and 165 MPa, respectively, indicating that the compressive strength decreased to half its value. Fig. 10b and c showed the effect of porosity and temperature on Young's modulus and yield stress, respectively. Porosity had a negative impact on both Young's modulus and yield stress (Karuppudaiyan et al., 2018), with the more decisive influence on yield stress. The porous composite scaffolds' elastic modulus values ranged between 3.30 and 20.50 GPa, depending on space holder content, mineral ratio, and sintering temperature. The scaffolds also exhibited compressive strength ~130–165 MPa at sintering temperature of 1000 °C or higher.

3.7. Numerical study

Numerical analyses of the (20,10) and (40,10) porous composite scaffolds were carried out to investigate the stress and strain distribution. These two scaffolds were chosen because of their mechanical

properties as ideal candidates for cortical bone substitutes. Analyses of the femur bone with the synthesised titanium scaffold (0,0) and the bone graft were also done for the purpose of comparing them to the mechanical behaviour of the porous composite scaffolds (20,10) and (40,10). Fig. 11 displays the equivalent von Mises stress of the femur bone with the scaffolds during normal standing up. The highest stress, measuring 57.62 MPa, was observed on the contact surfaces between the femoral shaft and titanium scaffold (0,0) (Fig. 12a). The model featuring a scaffold (20,10) had a maximum stress of 43.77 MPa (Fig. 11c), also on the contact surfaces but at a lower value than the titanium scaffold. The scaffold (40,10) (Fig. 12b) and the bone graft (Fig. 11b) had very similar stress results, with a maximum stress value of approximately 36 MPa distributed along the femoral shaft.

Fig. 13 illustrates a comparison of the equivalent elastic strain for the four models of the femur bone with the synthesised scaffolds during normal standing up. The strain distribution was along the femoral shaft, with the maximum value located closer to the distal part due to the fixed boundary conditions. On examining the strain distribution across the four scaffolds, it was observed that the titanium scaffold (0,0) generated only minor elastic strain (Fig. 13a). The strain distributions for the bone graft and (40,10) scaffold were similar, as depicted in Fig. 13b and d, respectively. The strain occurred along these two scaffolds with the highest value on the contact area between the lower surface of the scaffolds and the femoral shaft. The elastic strain generated along the bone graft during standing ranged from 0.24% to 0.61%, while for the (40,10) scaffold, it ranged from 0.18% to 0.56%. However, the elastic
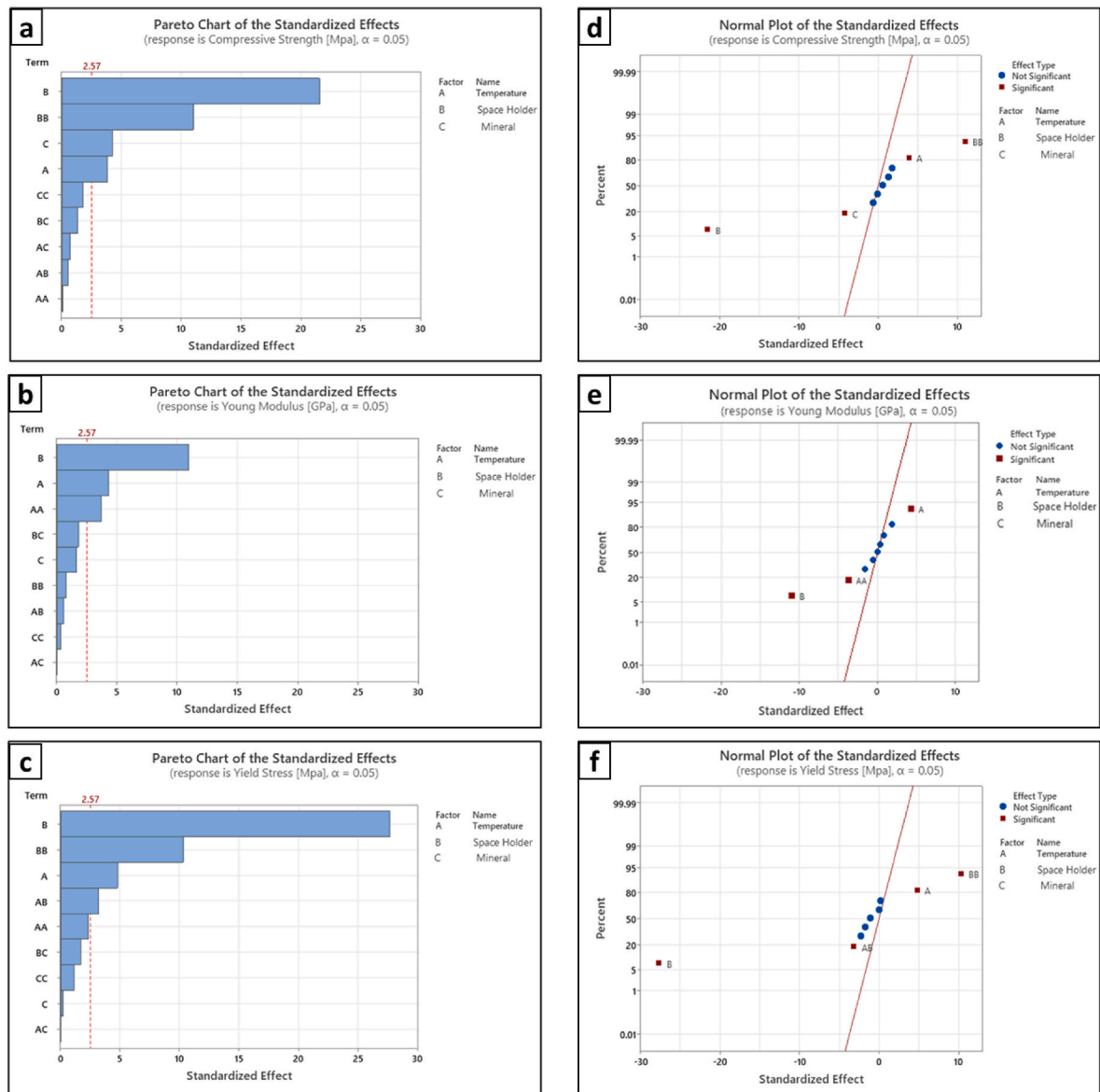
Fig. 9. Pareto charts (a,b,c) and normal plots (d,e,f) of the standardized effects of the fabrication variables on the compressive strength, Young modulus, and yield stress, respectively; α = 0.05.

strain along the (20,10) scaffold was ~0.12% (Fig. 13c), which was lower than strain value for the scaffold (40,10) as shown in (Fig. 13d).

4. Discussion

In this work, we demonstrate the design and fabrication of porous composite scaffolds (titanium/Fe^{3+} doped brushite) that can be functionalized to provide optimal biomechanical support. These scaffolds can be specifically designed for patients who may have experienced a femoral injury, taking into consideration their body mass index. Compositional and structural characterisations of the synthesised scaffolds demonstrate that the optimal scaffold designs are possible to realize in conjunction with the FEM and mechanical properties analysis. The resultant phases after sintering composite material (titanium with 10%vol Fe^{3+} dopped brushite) in argon at 1000 °C were hexagonal α-titanium and β-pyrophosphate (β-$Ca_2P_2O_7$). Beta pyrophosphate is considered a promising material for bone tissue engineering due to its significant role in hard tissue mineralisation, as demonstrated in previous studies (Atiyah et al., 2021; Anastasiou et al., 2019).

The powder metallurgy with a space holder methodology proved to

be effective in producing porous composite scaffolds with approximately 38–60% open porosity. The space holder approach offers an appropriate approach for controlling the physical contact between titanium particles for optimizing the porosity with respect to the need for overall load requirement and distribution along the length of a damaged femur. Furthermore, an increase in open porosity was observed in both solid composite samples (0,5) and (0,10) as well as porous samples (20,0), (20,5), and (20,10) when the DCPD-Fe mineral ratio was increased up to 10 vol%. This phenomenon can be attributed to the formation of small pores between titanium and DCPD-Fe particles. Notably, this effect was most significant in samples (40,0), (40,5), and (40,10), where an increase in the mineral ratio from 0 to 10 vol% led to a substantial rise in open porosity, from 55.40% to 60.00%. The open porosity of the synthesised porous scaffolds is promising for bone scaffolds, as it exceeds 30 vol%. The ideal structure for a bone scaffold should have porosity ranging from 30 to 90 vol%, according to literature (Dabrowski et al., 2010). The synthesised porous scaffolds, including samples (20,0), (20, 10), (40,0), and (40,10), exhibited an optimal pore size distribution ranging from 100 to 850 μm. It is important to note that for effective bone regeneration, bone scaffolds should have a minimum pore size
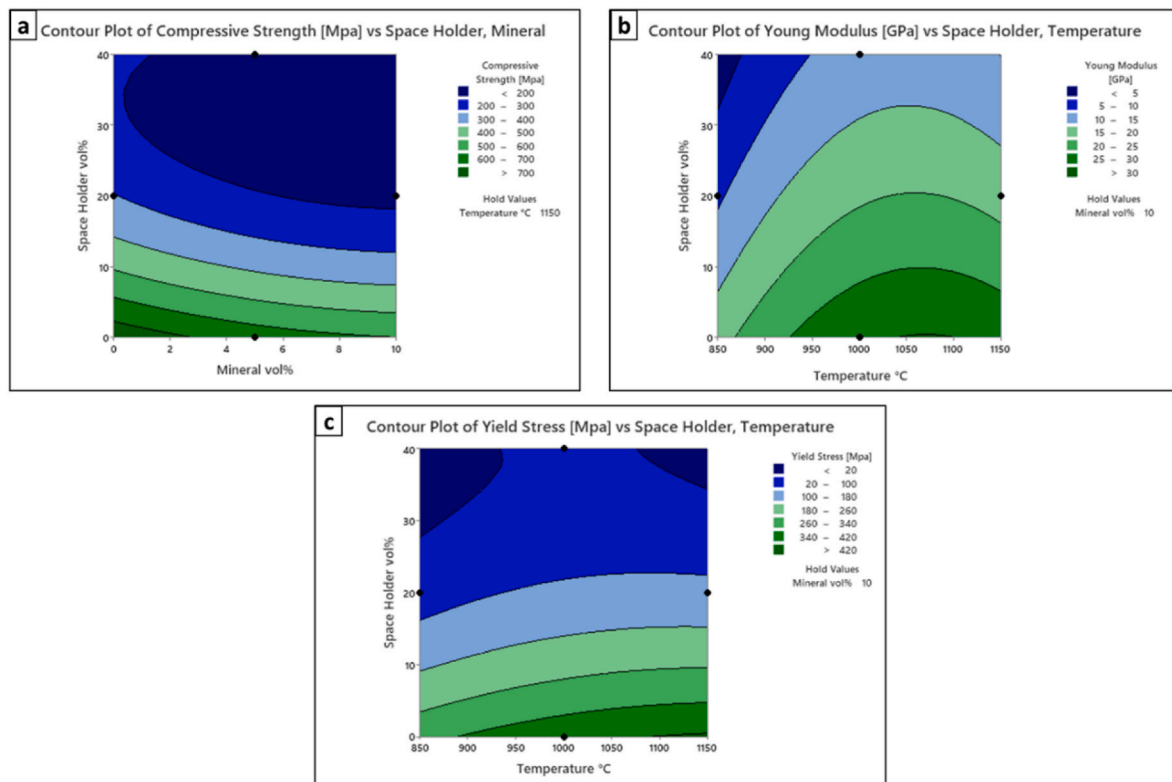
Fig. 10. 2D contour plots for: the effect of porosity and mineral ratio on compressive strength at a sintering temperature of 1150 °C (a), and the effect of porosity and sintering temperature on elastic modulus and yield stress when the mineral ratio is 10 vol% (b and c). The colours indicate the corresponding mechanical properties values.

falling within the range of 100–500 μm, as documented in multiple studies (Moreno et al., 2016; Bansiddhi et al., 2014; Bose et al., 2012; Gorth et al., 2011; Liverani et al., 2017; Abbasi et al., 2020; Nam et al., 2020; Han et al., 2021; Ikada, 2006; Costa-Pinto et al., 2011; Williams, 2008; Liu et al., 2004; Navarro et al., 2008; Krieghoff et al., 2019). The size of pores has a direct impact on the speed of new bone development, with larger pores promoting vascularization and accelerating osteogenesis. Additionally, the synthesised scaffolds featured smaller pores (<50 μm), which played a crucial role in providing interconnectivity throughout the entire structure. However, it's worth considering that excessively large pores can compromise the mechanical properties of the scaffold due to void volume, as indicated by previous research (Moreno et al., 2016; Bose et al., 2012; Ikada, 2006; Costa-Pinto et al., 2011; Williams, 2008; Liu et al., 2004; Navarro et al., 2008). Pore interconnectivity is another crucial factor for bone scaffolds, facilitating cell seeding, penetration, and migration of osteoblast cells into the scaffold (Moreno et al., 2016; Bose et al., 2012; Ikada, 2006; Costa-Pinto et al., 2011; Williams, 2008; Liu et al., 2004; Navarro et al., 2008). In our study, μCT analysis of the scaffold (40,10) revealed a remarkable pore interconnectivity, with approximately 95% of the pores being interconnected and accessible. These open and interconnected pores are pivotal for achieving stable fixation with surrounding tissue, creating a highly convoluted interface between the growing bone and the porous scaffold (Murphy et al., 2010; Karageorgiou et al., 2005; Kuboki et al., 2001; Roosa et al., 2010; Tsuruga et al., 1997). Moreover, open and interconnected pores facilitate the essential transport of nutrients and oxygen required during bone tissue growth (Bose et al., 2012; Bartoš et al., 2018; Nava et al., 2016; Chen et al., 2017b; Mercado-Pagán et al., 2015; Santos et al., 2010; Chiu et al., 2011; Feng et al., 2011). In contrast, scaffolds with a lower space holder percentage, such as the (20, 10) scaffold, exhibited reduced pore interconnectivity, with approximately 20% of pores rendered inaccessible. This limitation may hinder the scaffold's effectiveness in promoting new bone tissue ingrowth.

Other technologies such as 3D printing offers the potential to produce fully interconnective pore structures in a single material. However, it's important to recognize that 3D printing of metal-ceramic composites can be a complex process. Achieving success in this area requires cautious consideration of various factors including parameters, post-processing steps, and cost factors.

The elastic modulus of the porous composite scaffolds varied between 3.30 and 20.50 GPa, depending on porosity, mineral ratio, and sintering temperature. Remarkably, these values are in a comparable range to that of the human femur bone, which typically falls between 4 and 20 GPa, as documented in several studies (Öhman et al., 2011; Ajaxon et al., 2017; Bayraktar et al., 2004; Prochor et al., 2016). The scaffolds also exhibited adequate compressive strength ~130–165 MPa at sintering temperatures of 1000 °C or higher, similar to that reported for femur cortical bone (Öhman et al., 2011; Ajaxon et al., 2017; Havaldar et al., 2014; Johnson et al., 2011; Mohamed et al., 2015). The mechanical properties of the scaffolds were significantly influenced by the fabrication process using powder metallurgy with a space holder. The addition of DCPD-Fe mineral into pure titanium increased the porosity within the pressed and sintered structure, resulting in lower density values and decreased mechanical integrity. However, the intentional introduction of pores into the scaffold structure using either the space holder KCl or the DCPD-Fe particles played a crucial role in reducing stiffness to align with the natural bone's mechanical characteristics. It's important to note that while high porosity can increase the likelihood of micro-cracks or defects and reduce compressive strength, a careful a balance must be maintained during scaffold design and manufacturing to achieve an appropriate porous structure with optimal mechanical properties (Karuppudaiyan et al., 2018; Ajaxon et al., 2017; Wang et al., 2010). Furthermore, the addition of DCPD-Fe mineral to titanium helped moderate the stiffness of the scaffolds to match the cortical femoral bone without inducing stress localization due to excessive porosity (>70%), as reported in previous works (Kramschuster
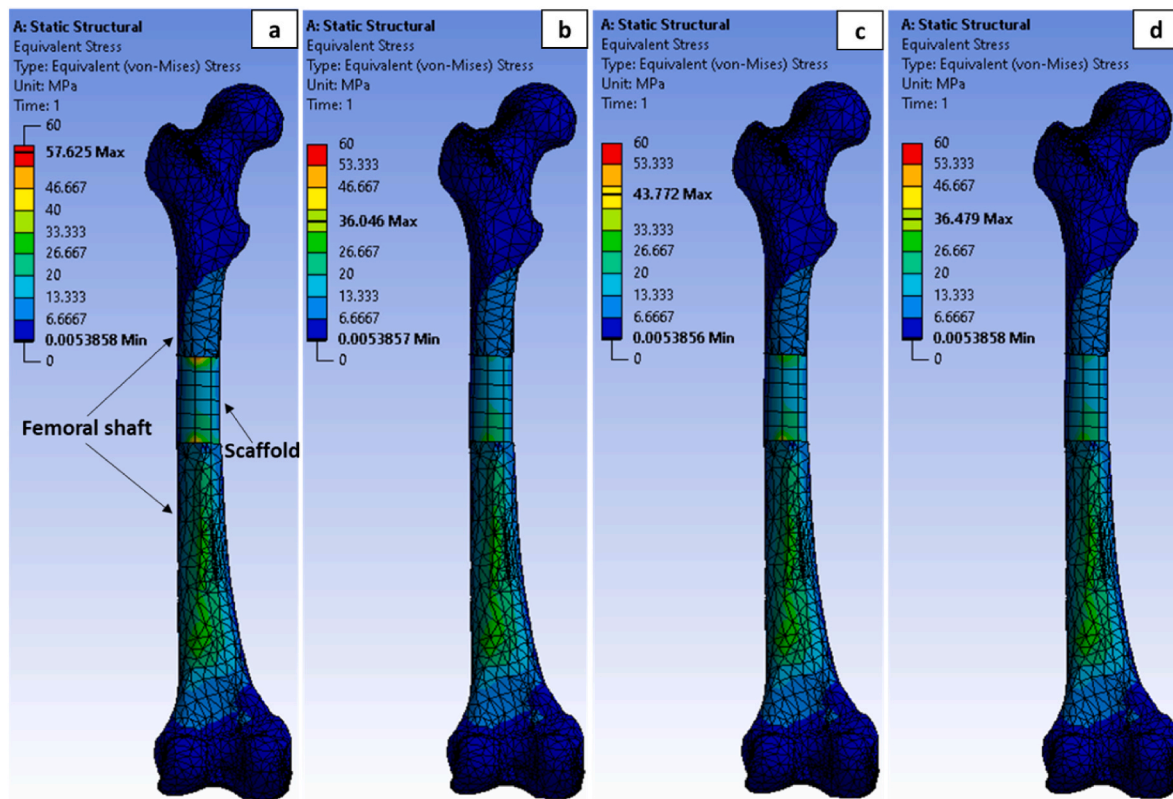
Fig. 11. The equivalent von Mises stress of a fractured mid-shaft femur with the synthesised scaffolds. The figure shows four different models: the pure titanium scaffold (0,0) (a), the bone graft (b), the (20,10) scaffold fabricated using 20%vol KCl and 10%vol DCPD-Fe (c), and the (40,10) scaffold fabricated using 40%vol KCl and 10% vol DCPD-Fe (d). The colour coding in the figure ranges from low values in blue to higher values in red.
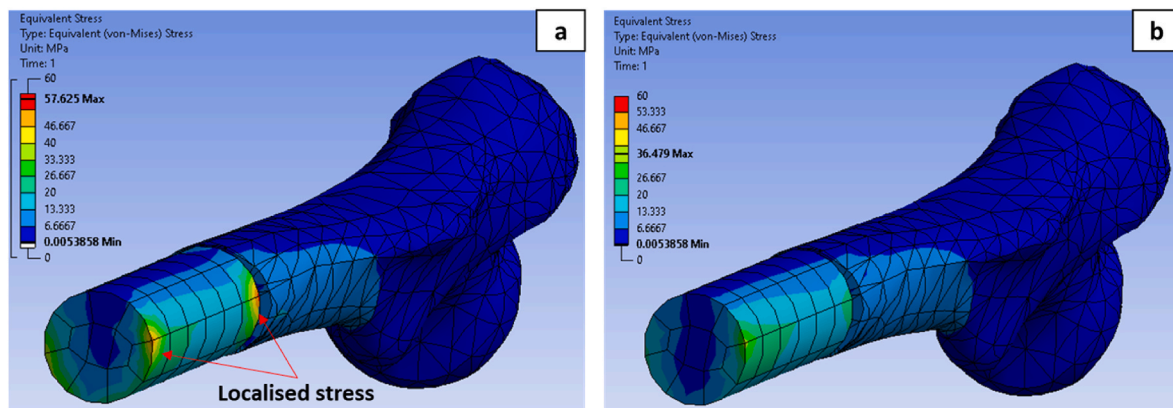

Fig. 12. The equivalent von Mises stress at the contact surfaces between the femoral shaft and pure titanium scaffold (0,0) in (a) and between the femoral shaft and (40,10) scaffold fabricated using 40%vol KCl and 10% vol DCPD-Fe in (b). The colour coding in the figure ranges from low values in blue to higher values in red.

et al., 2012; Gorth et al., 2011). The results also emphasized the crucial role of sintering temperature in achieving a delicate balance among mechanical properties, desired structure, and phase constitution. Increasing the sintering temperature significantly increased the elastic modulus, compressive strength, and yield stress through high-temperature diffusion, which improved particle bonding (Oh et al., 2011; Kwasniak et al., 2014; Luo et al., 2020; Ji et al., 2018; Qian et al., 2010; Gardner et al., 2021; Wu, 2013; Heaney et al., 2004; Moorhouse, 2013; Lindwall et al., 2018). However, it's noteworthy that sintering temperatures below 1000 °C may lead to structural instability when scaffolds are employed over a long time *in vivo*. For instance, at a sintering temperature of 850 °C, the scaffold (20,10) exhibited a compressive strength of 72 MPa, which is relatively low compared to

natural bone. In contrast, sintering the (20,10) scaffold at 1150 °C yielded a compressive strength of 165 MPa. This finding indicates that lower sintering temperatures may not provide the necessary structural integrity for long-term use due to poor interface bonding between particles at those lower temperatures (Oh et al., 2011; Kwasniak et al., 2014; Luo et al., 2020; Ji et al., 2018; Qian et al., 2010; Gardner et al., 2021; Wu, 2013; Heaney et al., 2004; Moorhouse, 2013; Lindwall et al., 2018). As this bonding process is thermally regulated, our research has determined the optimal sintering temperature to get the desired mechanical properties and also the required mineral phase (as depicted in Fig. 3) to be approximately 1000 °C.

The titanium scaffold (0,0) exhibited excessive stress and negligible strain, which markedly differed from the response observed in natural
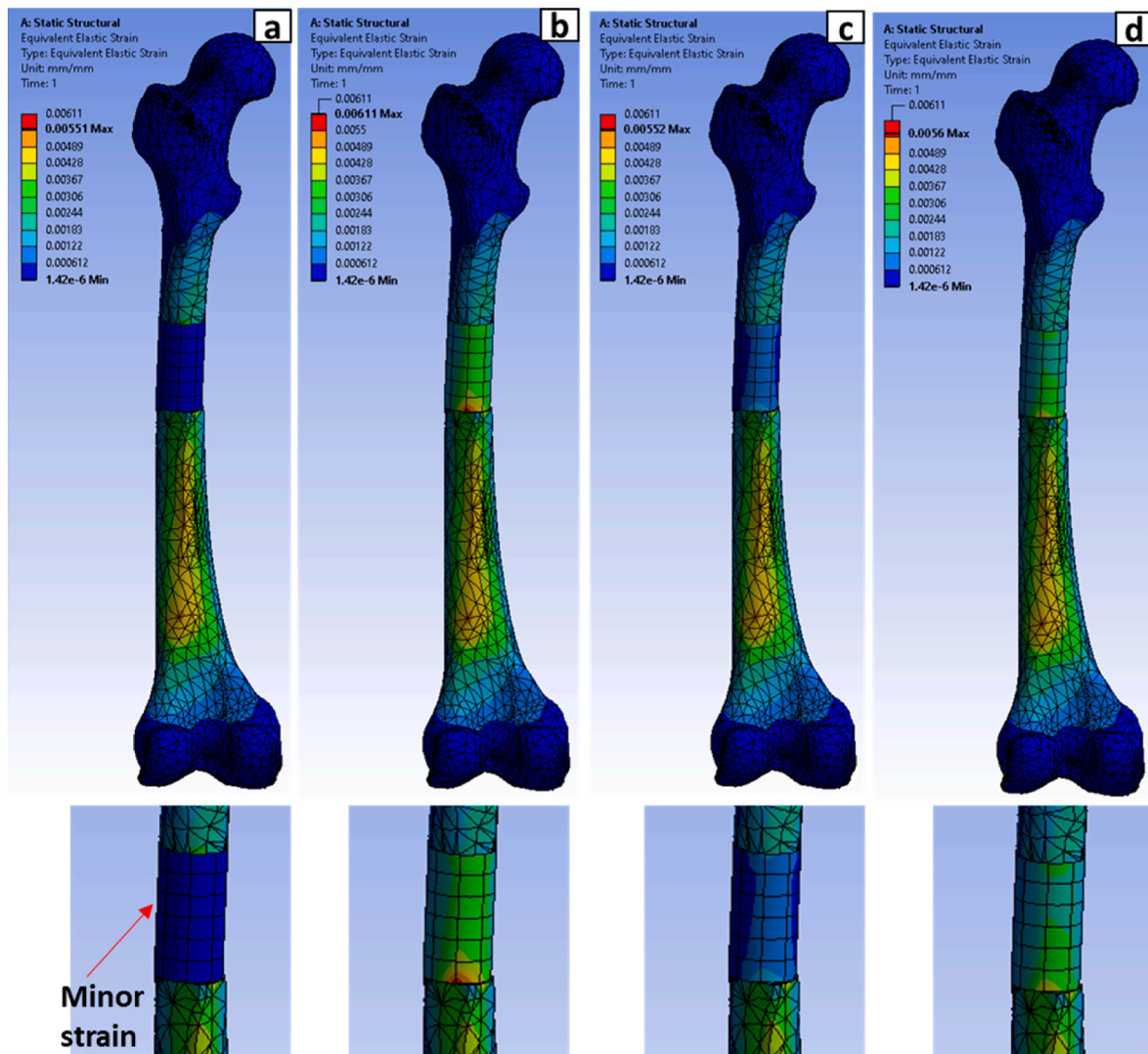
Fig. 13. Equivalent elastic strain of a fractured mid-shaft femur with the synthesised scaffolds. The figure shows four different models: the pure titanium scaffold (0,0) (a), the bone graft (b), the (20,10) scaffold fabricated using 20%vol KCl and 10%vol DCPD-Fe (c), and the (40,10) scaffold fabricated using 40%vol KCl and 10% vol DCPD-Fe (d). The colour coding in the figure ranges from low values in blue to higher values in red.

bone graft. This behaviour can be explained by Wolff's Law through a simple mechanical rule in the composite system consisting of the femoral shaft and scaffold. In this case, the stiffer component, represented by the titanium scaffold sustain the greater load, resulting in an overload of the scaffold and reduced loading on the femoral shaft due to the stiffness mismatch. This observing raises concerns about the potential for stress shielding, which could compromise the long-term stability of the scaffold, as documented in prior studies (Dapporto et al., 2017; Mi et al., 2007; Behrens et al., 2008). It is worth noting that bone tissue tends to proliferate more in regions subject to higher mechanical stress (loaded areas) and less in areas with lower stress levels (unloaded areas). This is an important consideration in scaffold design and application for bone repair, as ensuring proper load transfer and distribution can mitigate stress shielding and promote the growth of healthy bone tissue (Bayraktar et al., 2004; Havaldar et al., 2014; Johnson et al., 2011; Liu, 1997; Roohani-Esfahani et al., 2016). In contrast, the synthesised scaffolds (20,10) and (40,10) exhibited more favourable behaviour, resulting in lower stress levels and indicating a better match with the stiffness of the femoral shaft. These porous composite scaffolds (20,10) and (40,10) approached stiffness values closer to those of natural bone, reducing the risk of stress shielding and peri-scaffold bone resorption. Additionally, these scaffolds facilitated interface

scaffold-bone micromotions, which hold promise for osteointegration and bone ingrowth by stimulating cell responses. The scaffold's ability to respond to mechanical loading and deformation is essential for the proper functioning and long-term performance of scaffolds in bone repair applications, as highlighted in relevant literature (Amini et al., 2012; Pioletti, 2010; Zhu et al., 2021; Breuls et al., 2008; Fuchs et al., 2009; Lovald et al., 2012; Goharian, 2019; Shayesteh Moghaddam et al., 2016; Sivananthan et al., 2021; Giannoudis et al., 2005).

5. Conclusion

- The sintered composite material (titanium with 10%vol Fe^{3+} dopped brushite) demonstrated a phase composition consisting of α-titanium and β-pyrophosphate (β-$Ca_2P_2O_7$) which is well known for its excellent biocompatibility and osteoconductivity.
- Scaffolds (40,10) and (20,10) were selected for a comparative analysis. The (40,10) scaffold consists of 10 vol% DCPD-Fe mineral and 40 vol% KCl, while the (20,10) scaffold comprises 10 vol% DCPD-Fe mineral and 20 vol% KCl.
- The (40,10) and (20,10) scaffolds featured open and sufficiently large interconnected pores that can facilitate vascularization and the penetration of cells.

- The elastic moduli of the (40,10) and (20,10) scaffolds were 8.7 GPa and 20.17 GPa, respectively, when sintered in argon at temperatures equal to or greater than 1000 °C. These values are comparable to those of the human femur bone, indicating their capacity to reduce the stress-shielding effect.
- The (40,10) and (20,10) scaffolds also demonstrated suitable compressive strength, approximately 130 MPa and 165 MPa, respectively, when sintered in argon at temperatures equal to or greater than 1000 °C.
- The analysis of the relationships between compressive properties and the synthesis parameters of the fabricated scaffolds was conducted using response surface methodology (RSM), employing a three-factor Box-Behnken design (BBD).
- The numerical study provided evidence that the synthesised scaffolds (20,10) and (40,10) exhibit biomechanical flexibility when interacting with the surrounding bone. These scaffolds show promise in effectively supporting bone regeneration within critical-size defects by responding to mechanical loading and reducing stress shielding.

CRediT authorship contribution statement

Dina Abdulaziz: Writing – review & editing, Writing – original draft, Methodology, Investigation, Formal analysis, Data curation, Conceptualization. **Antonios D. Anastasiou:** Supervision. **Vasiliki Panagiotopoulou:** Supervision. **El Mostafa Raif:** Supervision. **Peter V. Giannoudis:** Supervision. **Animesh Jha:** Supervision.

Declaration of competing interest

The authors declare the following financial interests/personal relationships which may be considered as potential competing interests:
Dina Abdulaziz reports financial support was provided by Royal Commission for the Exhibition of 1851. Dina Abdulaziz has patent issued to PCT/GB 2022/050670.

Data availability

Data will be made available on request.

Acknowledgements

References

Abbasi, N., et al., 2020. Porous scaffolds for bone regeneration. J. Sci.: Advanced Materials and Devices 5 (1), 1–9.

Ajaxon, I., et al., 2017. Elastic properties and strain-to-crack-initiation of calcium phosphate bone cements: revelations of a high-resolution measurement technique. J. Mech. Behav. Biomed. Mater. 74, 428–437.

Alsubhe, E., et al., 2020. Analysis of the osteogenic and mechanical characteristics of iron (Fe2+/Fe3+)-doped β-calcium pyrophosphate. Mater. Sci. Eng. C 115, 111053.

Amini, A.R., Laurencin, C.T., Nukavarapu, S.P.J.C.R.i.B.E., 2012. Bone tissue engineering: recent advances and challenges. Crit. Rev. Biomed. Eng. 40 (5), 363–408.

Anastasiou, A., et al., 2016. Sintering of calcium phosphates with a femtosecond pulsed laser for hard tissue engineering. Mater. Des. 101, 346–354.

Anastasiou, A., et al., 2017. β-pyrophosphate: a potential biomaterial for dental applications. Mater. Sci. Eng. C 75, 885–894.

Anastasiou, A., et al., 2019. Drug loading capacity of microporous β-pyrophosphate crystals. Mater. Des. 168, 107661.

Andrzejowski, P., Giannoudis, P.V., 2019. The 'diamond concept'for long bone non-union management. J. Orthop. Traumatol. 20 (1), 1–13.

Arrington, E.D., et al., 1996. Complications of iliac crest bone graft harvesting. Clin. Orthop. Relat. Res. 329, 300–309.

Atiyah, A.G., Al-Falahi, N.H.R., Zarraq, G.A., 2021. Synthesis and characterization of porous β-calcium pyrophosphate bone scaffold derived from avian eggshell. Pakistan J. Zool. 1–4.

Balbinotti, P., et al., 2011. Microstructure development on sintered Ti/HA biocomposites produced by powder metallurgy. Mater. Res. 14 (3), 384–393.

Bansiddhi, A., et al., 2008. Porous NiTi for bone implants: a review. Acta Biomater. 4 (4), 773–782.

Bansiddhi, A., Dunand, D.C., 2014. Titanium and NiTi foams for bone replacement. In: Bone Substitute Biomaterials. Elsevier, pp. 142–179.

Bartoš, M., Suchý, T., Foltán, R., 2018. Note on the use of different approaches to determine the pore sizes of tissue engineering scaffolds: what do we measure? Biomed. Eng. Online 17 (1), 1–15.

Bayraktar, H.H., et al., 2004. Comparison of the elastic and yield properties of human femoral trabecular and cortical bone tissue. J. Biomech. 37 (1), 27–35.

Behrens, B.-A., et al., 2008. Numerical investigations of stress shielding in total hip prostheses. Proc. IME H J. Eng. Med. 222 (5), 593–600.

Bergh, C., et al., 2020. Fracture incidence in adults in relation to age and gender: a study of 27,169 fractures in the Swedish Fracture Register in a well-defined catchment area. PLoS One 15 (12), e0244291.

Bhatt, A., Parappagoudar, M., 2015. Modeling and analysis of mechanical properties in structural steel-DOE approach. Archives of Foundry Engineering 15 (4), 5–12.

Bhosale, R.S., Zambare, B., 2013. Sex determination from femur using length of femur in Maharashtra. J. Dent. Med. Sci. 3 (4), 1–3.

Bose, S., Roy, M., Bandyopadhyay, A., 2012. Recent advances in bone tissue engineering scaffolds. Trends Biotechnol. 30 (10), 546–554.

Breuls, R.G., Jiya, T.U., Smit, T.H., 2008. Scaffold stiffness influences cell behavior: opportunities for skeletal tissue engineering. Open Orthop. J. 2, 103–109.

Calori, G.M., Giannoudis, P.V., 2011. Enhancement of fracture healing with the diamond concept: the role of the biological chamber. Injury 42 (11), 1191–1193.

Chen, Q., Thouas, G.A., 2015. Metallic implant biomaterials. Mater. Sci. Eng. R Rep. 87, 1–57.

Chen, Y., et al., 2017a. Manufacturing of graded titanium scaffolds using a novel space holder technique. Bioact. Mater. 2 (4), 248–252.

Chen, Y., et al., 2017b. Mechanical properties and biocompatibility of porous titanium scaffolds for bone tissue engineering. J. Mech. Behav. Biomed. Mater. 75, 169–174.

Cheppudira Thimmaiah, P., et al., 2018. A new approach to compute the porosity and surface roughness of porous coated capillary-assisted low pressure evaporators. Sci. Rep. 8 (1), 1–11.

Chiarello, E., et al., 2013. Autograft, allograft and bone substitutes in reconstructive orthopedic surgery. Aging Clin. Exp. Res. 25 (1), 101–103.

Chiu, Y.-C., et al., 2011. The role of pore size on vascularization and tissue remodeling in PEG hydrogels. Biomaterials 32 (26), 6045–6051.

Clavell, R.S., et al., 2016. In vitro assessment of the biological response of Ti6Al4V implants coated with hydroxyapatite microdomains. J. Biomed. Mater. Res. 104 (11), 2723–2729.

Costa-Pinto, A.R., Reis, R.L., Neves, N.M., 2011. Scaffolds based bone tissue engineering: the role of chitosan. Tissue Eng. B Rev. 17 (5), 331–347.

Dabrowski, B., et al., 2010. Highly porous titanium scaffolds for orthopaedic applications. J. Biomed. Mater. Res. B Appl. Biomater. 95 (1), 53–61.

Dapporto, M., Tampieri, A., Sprio, S., 2017. Composite calcium phosphate/titania scaffolds in bone tissue engineering. In: Application of Titanium Dioxide, pp. 43–59.

Das, K., et al., 2008. Surface modification of laser-processed porous titanium for load-bearing implants. Scripta Mater. 59 (8), 822–825.

Davis, J., 2003a. Materials for Medical Devices. ASM Handbook Series.

Davis, J., 2003b. Handbook of Materials for Medical Devices. ASM Handbook Series.

Dehghan-Manshadi, A., et al., 2018. Porous titanium scaffolds fabricated by metal injection moulding for biomedical applications. Materials 11 (9), 1573.

Eliaz, N., Metoki, N., 2017. Calcium phosphate bioceramics: a review of their history, structure, properties, coating technologies and biomedical applications. Materials 10 (4), 334.

Elmadani, E., et al., 2012. Characterization of rare-earth oxide photoactivated calcium phosphate minerals for resurfacing teeth. J. Am. Ceram. Soc. 95 (9), 2716–2724.

Elsalanty, M.E., Genecov, D.G., 2009. Bone grafts in craniofacial surgery. Craniomaxillofacial Trauma Reconstr. 2 (3–4), 125–134.

Fallah, A., et al., 2022. 3D printed scaffold design for bone defects with improved mechanical and biological properties. J. Mech. Behav. Biomed. Mater. 134, 105418.

Feller, L., et al., 2014. Osseointegration: biological events in relation to characteristics of the implant surface. South African Dental Journal 69 (3), 112–117.

Feng, B., et al., 2011. The effect of pore size on tissue ingrowth and neovascularization in porous bioceramics of controlled architecture in vivo. Biomed. Mater. 6 (1), 015007.

Floroiana, L., et al., 2007. Synthesis and characterization of bioglass thin films. Dig. J. Nanomater. Biostruct. 2 (3), 285–291.

Fuchs, R.K., Warden, S.J., Turner, C.H., 2009. Bone anatomy, physiology and adaptation to mechanical loading. In: Bone Repair Biomaterials. Elsevier, pp. 25–68.

Gardner, H., et al., 2021. Quantifying the effect of oxygen on micro-mechanical properties of a near-alpha titanium alloy. J. Mater. Res. 36 (12), 2529–2544.

Ghassemi, T., et al., 2018. Current concepts in scaffolding for bone tissue engineering. Arch. Bone Joint Surg. 6 (2), 90.

Giannoudis, P.V., Dinopoulos, H., Tsiridis, E., 2005. Bone substitutes: an update. Injury 36 (3), S20–S27.

Giannoudis, P.V., Einhorn, T.A., Marsh, D., 2007. Fracture healing: the diamond concept. Injury 38, S3–S6.

Giannoudis, P.V., et al., 2008. The diamond concept–open questions. Injury 39, S5–S8.

Giannoudis, P.V., et al., 2016. Restoration of long bone defects treated with the induced membrane technique: protocol and outcomes. Injury 47, S53–S61.

Goharian, A., 2019. Osseointegration of Orthopaedic Implants. Academic Press.

Gorth, D., Webster, T., 2011. Matrices for tissue engineering and regenerative medicine. In: Biomaterials for Artificial Organs. Elsevier, pp. 270–286.

Han, Y., et al., 2021. Effect of pore size on cell behavior using melt electrowritten scaffolds. Front. Bioeng. Biotechnol. 9, 495.

Havaldar, R., Pilli, S., Putti, B., 2014. Insights into the effects of tensile and compressive loadings on human femur bone. Adv. Biomed. Res. 3.

He, S., et al., 2012. Response surface methodology optimization of fermentation conditions for rapid and efficient accumulation of macrolactin A by marine Bacillus amyloliquefaciens ESB-2. Molecules 18 (1), 408–417.

Heaney, D.F., German, R., 2004. Advances in the sintering of titanium powders. Euro PM2004.

Hench, L.L., Jones, J.R., 2015. Bioactive glasses: frontiers and challenges. Front. Bioeng. Biotechnol. 3, 194.

Ho, S.T., Hutmacher, D.W., 2006. A comparison of micro CT with other techniques used in the characterization of scaffolds. Biomaterials 27 (8), 1362–1376.

Hubbe, U., et al., 2022. A fully ingrowing implant for cranial reconstruction: results in critical size defects in sheep using 3D-printed titanium scaffold. Biomater. Adv. 136, 212754.

Ibrahim, M.Z., et al., 2017. Biomedical materials and techniques to improve the tribological, mechanical and biomedical properties of orthopedic implants–A review article. J. Alloys Compd. 714, 636–667.

Ikada, Y., 2006. Challenges in tissue engineering. J. R. Soc. Interface 3 (10), 589–601.

Ji, X., et al., 2018. Effect of oxygen addition on microstructures and mechanical properties of Ti-7.5 Mo alloy. J. Alloys Compd. 737, 221–229.

Johansen, A., et al., 2014. 48 Using the national hip fracture database (NHFD) to profile the impact of hip fracture on the NHS. Age Ageing 43 (Suppl. l_2) ii13-ii13.

Johnson, A.J.W., Herschler, B.A., 2011. A review of the mechanical behavior of CaP and CaP/polymer composites for applications in bone replacement and repair. Acta Biomater. 7 (1), 16–30.

Kanis, J., et al., 2000. Risk of hip fracture according to the World Health Organization criteria for osteopenia and osteoporosis. Bone 27 (5), 585–590.

Karageorgiou, V., Kaplan, D., 2005. Porosity of 3D biomaterial scaffolds and osteogenesis. Biomaterials 26 (27), 5474–5491.

Karuppudaiyan, S., Singh, D.K.J., Santosh, V.M., 2018. Finite element analysis of scaffold for large defect in femur bone. In: IOP Conference Series: Materials Science and Engineering. IOP Publishing.

Kramschuster, A., Turng, L.-S., 2012. 17—fabrication of tissue engineering scaffolds. In: Handbook of Biopolymers and Biodegradable Plastics: Properties, Processing and Applications.

Krieghoff, J., et al., 2019. Increased pore size of scaffolds improves coating efficiency with sulfated hyaluronan and mineralization capacity of osteoblasts. Biomater. Res. 23 (1), 1–13.

Kuboki, Y., Jin, Q., Takita, H., 2001. Geometry of carriers controlling phenotypic expression in BMP-induced osteogenesis and chondrogenesis. JBJS 83 (1_Suppl. l_2), S105–S115.

Kumar, K.N., et al., 2015. Biomechanical stress analysis of a human femur bone using ANSYS. Mater. Today: Proc. 2 (4–5), 2115–2120.

Kunisch, E., et al., 2023. A comparative in vitro and in vivo analysis of the biological properties of the 45S5-, 1393-, and 0106-B1-bioactive glass compositions using human bone marrow-derived stromal cells and a rodent critical size femoral defect model. Biomater. Adv., 213521

Kwasniak, P., et al., 2014. Influence of oxygen content on the mechanical properties of hexagonal Ti—first principles calculations. Mater. Sci. Eng., A 590, 74–79.

Levine, B.R., Fabi, D.W., 2010. Porous metals in orthopedic applications – a review. Mater. Werkst. 41 (12), 1001–1010.

Lindwall, G., et al., 2018. The effect of oxygen on phase equilibria in the Ti-V system: impacts on the AM processing of Ti alloys. JOM 70 (9), 1692–1705.

Liu, D.M., 1997. Influence of Porosity and Pore Size on the Compressive Strength of Porous Hydroxyapatite Ceramic, vol. 23, pp. 135–139, 2.

Liu, X., Ma, P.X., 2004. Polymeric scaffolds for bone tissue engineering. Ann. Biomed. Eng. 32 (3), 477–486.

Liu, P., Chen, G.-F., 2014. Chapter three - application of porous metals. In: Porous Materials: Processing and Applications. Elsevier, pp. 113–188.

Liu, Q., Lu, W.F., Zhai, W., 2022. Toward stronger robocast calcium phosphate scaffolds for bone tissue engineering: a mini-review and meta-analysis. Biomater. Adv. 134, 112578.

Liverani, L., Roether, J., Boccaccini, A., 2017. Nanofiber composites in bone tissue engineering. In: Nanofiber Composites for Biomedical Applications. Elsevier, pp. 301–323.

Lovald, S., Kurtz, S.M., 2012. Applications of polyetheretherketone in trauma, arthroscopy, and cranial defect repair. In: PEEK Biomaterials Handbook. William Andrew Publishing, pp. 243–260.

Lowe, J.A., Fischer, S.J., 2018. Femur Shaft Fractures-Broken Thighbone. OrthoInfo.

Luo, S., et al., 2020. High oxygen-content titanium and titanium alloys made from powder. J. Alloys Compd. 836, 155526.

Ma, R., et al., 2016. Osseointegration of nanohydroxyapatite-or nano-calcium silicate-incorporated polyetheretherketone bioactive composites in vivo. Int. J. Nanomed. 11, 6023.

Mahmoudi, M., 2017. Femur Bone. GrabCAD Community.

Mandal, A., Roy, P., 2006. Modeling the compressive strength of molasses–cement sand system using design of experiments and back propagation neural network. J. Mater. Process. Technol. 180 (1–3), 167–173.

McIntosh, A., Jablonski, W., 1956. X-ray diffraction powder patterns of calcium phosphates. Anal. Chem. 28 (9), 1424–1427.

Mercado-Pagán, Á.E., et al., 2015. Vascularization in bone tissue engineering constructs. Ann. Biomed. Eng. 43 (3), 718–729.

Mi, Z.R., et al., 2007. Problem of stress shielding and improvement to the hip Implat designs: a review. J. Med. Sci. 7 (3), 460–467.

Miller, C.P., Chiodo, C.P., 2016. Autologous bone graft in foot and ankle surgery. Foot Ankle Clin. 21 (4), 825–837.

Mohamed, S., Shamaz, B.H., 2015. Bone tissue engineering and bony scaffolds. Int. J. Dent. Oral Health 1, 15–20.

Moorhouse, B., 2013. Controlling the Interstitial Element Concentration in Ti-6Al-4V Using Calciothermic Reduction. Imperial College London.

Moreno, M., et al., 2016. Scaffolds for bone regeneration: state of the art. Curr. Pharmaceut. Des. 22 (18), 2726–2736.

Mozafari, M., Sefat, F., Atala, A., 2019. Handbook of Tissue Engineering Scaffolds: Volume One. Woodhead Publishing.

Murphy, C.M., Haugh, M.G., O'brien, F.J., 2010. The effect of mean pore size on cell attachment, proliferation and migration in collagen–glycosaminoglycan scaffolds for bone tissue engineering. Biomaterials 31 (3), 461–466.

Nam, J.H., et al., 2020. Validation of the optimal scaffold pore size of nasal implants using the 3-dimensional culture technique. Arch. Plastic Surg. 47 (4), 310.

National Hip Fracture Database, Annual Report, 2017. Royal College of Physicians, London. RCP).

National Hip Fracture Database (NHFD), Annual Report, 2018. Royal College of Physicians, London. RCP).

National Hip Fracture Database (NHFD) Annual Report 2019, 2019.

Nauth, A., et al., 2018. Critical-size bone defects: is there a consensus for diagnosis and treatment? J. Orthop. Trauma 32, S7–S11.

Nava, M.M., et al., 2016. The effect of scaffold pore size in cartilage tissue engineering. J. Appl. Biomater. Funct. Mater. 14 (3), e223–e229.

Navarro, M., et al., 2008. Biomaterials in orthopaedics. J. R. Soc. Interface 5 (27), 1137–1158.

Nazirkar, G., et al., 2014. Effortless effort in bone regeneration: a review. J. Int. Oral Health: JIOH 6 (3), 120.

O'brien, F.J., 2011. Biomaterials & scaffolds for tissue engineering. Mater. Today 14 (3), 88–95.

Oh, J.-M., et al., 2011. Oxygen effects on the mechanical properties and lattice strain of Ti and Ti-6Al-4V. Met. Mater. Int. 17 (5), 733–736.

Öhman, C., et al., 2011. Compressive behaviour of child and adult cortical bone. Bone 49 (4), 769–776.

Pioletti, D.P., 2010. Biomechanics in bone tissue engineering. Comput. Methods Biomech. Biomed. Eng. 13 (6), 837–846.

Piveteau, L.-D., et al., 1999. Thin films of calcium phosphate and titanium dioxide by a sol-gel route: a new method for coating medical implants. J. Mater. Sci. Mater. Med. 10 (3), 161–167.

Prochor, P., Piszczatowski, S., Sajewicz, E., 2016. Biomechanical evaluation of a novel Limb Prosthesis Osseointegrated Fixation System designed to combine the advantages of interference-fit and threaded solutions. Acta Bioeng. Biomech. 18 (4), 21–31.

Qasim, M., et al., 2016. Patient-specific finite element estimated femur strength as a predictor of the risk of hip fracture: the effect of methodological determinants. Osteoporos. Int. 27 (9), 2815–2822.

Qian, M., Schaffer, G., Bettles, C., 2010. Sintering of titanium and its alloys. In: Sintering of Advanced Materials. Elsevier, pp. 324–355.

Roohani-Esfahani, S.I., Newman, P., Zreiqat, H., 2016. Design and Fabrication of 3D Printed Scaffolds with a Mechanical Strength Comparable to Cortical Bone to Repair Large Bone Defects. Scientific Reports.

Roosa, S.M.M., et al., 2010. The pore size of polycaprolactone scaffolds has limited influence on bone regeneration in an in vivo model. J. Biomed. Mater. Res. Part A: An Official Journal of The Society for Biomaterials, The Japanese Society for Biomaterials, and The Australian Society for Biomaterials and the Korean Society for Biomaterials 92 (1), 359–368.

Santos, M.I., Reis, R.L., 2010. Vascularization in bone tissue engineering: physiology, current strategies, major hurdles and future challenges. Macromol. Biosci. 10 (1), 12–27.

Schemitsch, E.H., 2017. Size matters: defining critical in bone defect size! J. Orthop. Trauma 31, S20–S22.

Schüpbach, P., et al., 2005. The Human Bone-Oxidized Titanium Implant Interface: A Light Microscopic, Scanning Electron Microscopic, Back-Scatter Scanning Electron Microscopic, and Energy-Dispersive X-Ray Study of Clinically Retrieved Dental Implants. Clinical Implant Dentistry and Related Research.

Semel, F., Lados, D., 2006. Porosity analysis of PM materials by helium pycnometry. Powder Metall. 49 (2), 173–182.

Shayesteh Moghaddam, N., et al., 2016. Metals for bone implants: safety, design, and efficacy. Biomanuf. Rev. 1 (1), 1–16.

Sheikh, M.S.A., Ganorkar, A., Dehankar, R., 2016. Finite element analysis of femoral intramedullary nailing. J. Res. Vol. 2 (10), 2395–7549.

Sidambe, A.T., 2014. Biocompatibility of advanced manufactured titanium implants—a review. Materials 7 (12), 8168–8188.

Sivananthan, S., Goodman, S., Burke, M., 2021. Failure mechanisms in joint replacement. In: Joint Replacement Technology. Elsevier, pp. 373–402.

Svedbom, A., et al., 2013. Osteoporosis in the European Union: a compendium of country-specific reports. Arch. Osteoporosis 8 (1–2), 137.

Tang, D., et al., 2016. Biofabrication of bone tissue: approaches, challenges and translation for bone regeneration. Biomaterials 83, 363–382.

Teimoori, M., Nokhbatolfoghahaei, H., Khojasteh, A., 2023. Bilayer scaffolds/ membranes for bone tissue engineering applications: a systematic review. Biomater. Adv., 213528

Toshima, T., et al., 2014. Morphology control of brushite prepared by aqueous solution synthesis. J. Asian Ceram. Soc. 2 (1), 52–56.

Tsuruga, E., et al., 1997. Pore size of porous hydroxyapatite as the cell-substratum controls BMP-induced osteogenesis. J. Biochem. 121 (2), 317–324.

Tuan, H.S., Hutmacher, D.W., 2007. The biomedical applications of computed tomography. In: Biomechanical Systems Technology: Volume 1: Computational Methods. World Scientific, pp. 193–223.

Tyas, B., Wilkinson, M., Singisetti, K., 2021. Effect of Covid-19 on best practice care of hip fracture patients: an analysis from the National Hip Fracture Database (NHFD). Surgeon 19 (5), e298–e303.

Voss, J.O., et al., 2022. Treatment options for critical size defects-Comparison of different materials in a calvaria split model in sheep. Biomater. Adv. 136, 212788.

Walsh, W.R., et al., 2017. Critical size bone defect healing using collagen–calcium phosphate bone graft materials. PLoS One 12 (1), e0168883.

Wang, H., 2004. Hydroxyapatite Degradation and Biocompatibility. The Ohio State University.

Wang, H., Fang, Z.Z., Sun, P., 2010. A critical review of mechanical properties of powder metallurgy titanium. Int. J. Powder Metall. 46 (5), 45–57.

Webb, P.A., 2001. Volume and density determinations for particle technologists. Micromerit. Instrument Corp 2 (16), 1.

Williams, D.F., 2008. On the mechanisms of biocompatibility. Biomaterials 29 (20), 2941–2953.

Woloszyk, A., et al., 2023. Biomimetic hematoma delivers an ultra-low dose of rhBMP-2 to successfully regenerate large femoral bone defects in rats. Biomater. Adv. 148, 213366.

Wu, H., 2013. Oxygen Diffusion through Titanium and Other Hcp Metals. University of Illinois at Urbana-Champaign.

Yang, X., et al., 2017. Characterization of the absolute volume change of cement pastes in early-age hydration process based on helium pycnometry. Construct. Build. Mater. 142, 490–498.

Yousif, A., Aziz, M., 2012. Biomechanical Analysis of the human femur bone during normal walking and standing up. IOSR J. Eng. 2 (8), 13–19.

Yun, Y., et al., 2009. Revolutionizing biodegradable metals. Mater. Today 12 (10), 22–32.

Zhang, Y., et al., 2022. Mechanically enhanced composite hydrogel scaffold for in situ bone repairs. Biomater. Adv. 134, 112700.

Zhao, Y., et al., 2023. Porous hydroxyapatite scaffold orchestrated with bioactive coatings for rapid bone repair. Biomater. Adv. 144, 213202.

Zhou, H., Lee, J., 2011. Nanoscale hydroxyapatite particles for bone tissue engineering. Acta Biomater. 7 (7), 2769–2781.

Zhu, G., et al., 2021. Bone physiological microenvironment and healing mechanism: basis for future bone-tissue engineering scaffolds. Bioact. Mater. 6 (11), 4110–4140.

Zimmermann, G., Moghaddam, A., 2011. Allograft bone matrix versus synthetic bone graft substitutes. Injury 42, S16–S21.